Multi-nuclear NMR of axially chiral biaryls in polypeptide orienting solvents: spectral discriminations and enantiorecognition mechanisms

Philippe Berdagué,[a] Jose-Enrique Herbert-Pucheta,[a] Vishwajeet Jha,[b] Armen Panossian,[b] Frédéric R. Leroux,[b] and Philippe Lesot[a]*

[a]*Laboratoire de RMN en Milieu Orienté, Université Paris Sud, Institut de Chimie Moléculaire et des Matériaux d'Orsay, UMR CNRS 8182, 91405 Orsay, France.*

[b]*Laboratoire de Chimie Moléculaire, Université de Strasbourg, UMR CNRS 7509, ECPM, 25 Rue Becquerel, 67087 Strasbourg, France.*

E-mail : philippe.lesot@u-psud.fr ; Tel.: +33 (0)1 69 15 47 59; Fax : +33 (0)1 69 15 81 05

ELECTRONIC SUPPLEMENTARY INFORMATION: INDEX

ELECTRONIC SUPPLEMENTARY INFORMATION: TEXT & DATA

I. Further information: background on NMR in CLC, further experimental and analytical details

I.1 Brief background of NMR in CLC

In contrast to liquid phases, compounds dissolved within homogeneous, uniform liquid crystals adopt a macroscopic orientation under the effect of the magnetic field, $\mathbf{B_o}$.[1] Consequently, all order-sensitive NMR interactions, such as chemical shift anisotropy (H_σ^{aniso}), dipolar couplings (H_D) or quadrupolar couplings (H_Q) (for spin I > 1/2) are no longer motionally averaged to zero.[2,3] Compared to isotropic NMR spectra, the presence of anisotropic interactions leads to spectral modifications as schematically depicted in **Figure 3**.

When the liquid crystal is chiral (CLC), the intermolecular interactions between each enantiomer and the CLC differ (when oriented in the magnetic field of the spectrometer), and their molecular orientations (and subsequently the internuclear vectors, i-j) are not the same on average ($S^S_{\alpha,\beta} \neq S^R_{\alpha,\beta}$ leading to $S^S_{i\text{-}j} \neq S^R_{i\text{-}j}$).[2] Due to the breaking of symmetry in CLC for ordering, same situation arises for enantiotopic directions (internuclear vectors) in prochiral molecules, and we have $S^{pro\text{-}S}_{i\text{-}j} \neq S^{pro\text{-}R}_{i\text{-}j}$.[4] In both cases, spectral modifications are expected when comparing NMR spectra/signals recorded with chiral and achiral liquid crystal (ALC). Generally a doubling of the spectral information/patterns for a given nuclear site indicates that the enantiorecognition phenomena occur and are revealed by NMR (see **Figure SI-1**).

Specifically dedicated to the analysis of organosoluble chiral analytes, homopolypeptide lyotropic CLC appear to be the most useful and efficient weakly orienting chiral mesophases for five primary reasons: i) all components are commercially available (polypeptide, organic co-solvent); ii) different types of homopolypeptides (or a mixture of them) can be used (PBLG, PCBLL or PELG)[5]; iii) a large panel of organic co-solvents (from apolar systems to polar aprotic ones) can be used, whereas their choice mainly depends on the solubility properties of analytes; iv) the approach does not request any specific polar groups in solutes (contrarily to almost all of classical NMR methods), and hence it can be applied to a wide variety of analytes (from alkanes to charged organometallic complexes); v) spectral enantiodiscriminations can be revealed from any magnetically active nuclei present in the molecules.[6]

I.2 1D-NMR *versus* 2D-NMR experiments

Initially developed using 1D-NMR on deuterated labeled solutes,[7] this methodology has been successfully extended from isolated but 100% abundant nuclei such as ^{19}F or ^{31}P,[8,9] to nuclei at low natural abundance such as ^{13}C (1.10 %) or ^{2}H (1.55 $\times$ 10^{-2} %).[10,11] The analytical interest of working with highly abundant nuclei such as ^{1}H is partly moderated by the important number of short- and long-range ^{1}H-^{1}H dipolar couplings that generally obscure the spectra and/or lead to low-resolution spectral patterns. Adapted solutions to record site-specific resolved spectra such as selective excitation 2D-NMR experiments (SERF)[12] and more recently the spatially encoded selective 2D techniques (along Z-direction)[12,13] exist. Although several variations of these experiments have been proposed to improve their robustness, the experiment set up is far to be trivial, while the analysis of second order spin systems remains an arduous task.[13] These approaches will not be explored in the present study.

Disregarding the sensitivity aspects, proton-decoupled NMR of very weakly abundant nuclei as ^{13}C or ^{2}H is advantageous because the detection of isotopomers containing two mutually interacting nuclei (scalar and dipolar coupling) is experimentally difficult or still impossible to be detected. Note however that first NMR detections of ^{13}C-^{2}H (enantio)-isotopomers were reported in 2012.[14] On the other hand, the analysis of their NMR spectra is facilitated compared to ones of strongly abundant nuclei. Beside this, and contrarily to NMR of specifically labeled molecules, all molecular sites are potential sites where spectral enantiodiscriminations can be revealed. As a racemic mixture is generally regarded first, the nuclear site showing the best spectral discriminations can be then selected to measure the enantiomeric excess in enantioenriched series.

Interestingly ^{13}C-{^{1}H} 1D-NMR spectra in ALC are a sum of single resonances associated to each inequivalent ^{13}C site whereas pairs of lines are observed in CLC if enantiodiscrimination on the basis of ^{13}C CSA difference occurs (see **Figure 3**). The large range of dispersion of ^{13}C chemical shifts (0 to 200 ppm) is advantageous to reduce/avoid excessive overlaps of ^{13}C lines, and a simple comparison with the isotropic ^{13}C-{^{1}H} 1D-NMR spectrum generally enables to rapidly assess the sites showing a chiral separation.[7] The analytical situation is more complex for Natural Abundance Deuterium NMR (NAD NMR) because spectra exhibit a sum of quadrupolar doublets (QD) associated to each inequivalent ^{2}H site. In CLC, two QDs are expected to be detected for each discriminated ^{2}H site. Even for small-sized molecules, numerous peaks overlap and doublet tangling can lead to undecipherable NMR results. This complexity originates from: i) the number of doublets; ii) the variation of quadrupolar splittings ($\Delta\nu_Q$) from one site to another one (from 0 to 500 Hz, generally); and iii) a rather low ^{2}H chemical dispersion (0 to 13 ppm). Contrarily to ^{13}C-{^{1}H} 1D-NMR, analysis of complex NAD NMR spectra is facilitated by recording 2D experiments able to correlate the two components of each ^{2}H QD (QUOSY-type experiments).[11,15] This in turn helps to assign them on the basis of their chemical shifts. Due to the very low sensitivity of NAD NMR, workable results are generally obtained when sufficient amounts of enantiomeric mixture (60-100 mg) are available, in particular for analytes of high molecular weight.

If the proton broadband decoupling greatly simplifies the analysis of NMR spectra of X nuclei, it removes all heteronuclear dipolar couplings, ^{1}H-X, that are also sensitive to the differential ordering of enantiomers, and so might be used to reveal enantiodiscriminations. Due to the small magnitude of ^{1}H-^{2}H dipolar couplings (< 1-2 Hz) originating from the low $\gamma(^{2}H)$ and small order parameters of solute (S = 10^{-3} to 10^{-5}), proton-coupled ^{2}H NMR is weakly relevant in practice, and has never been applied, so far. In contrast, proton-coupled ^{13}C NMR can provide a possible alternative to ^{13}C-{^{1}H} NMR in particular when the molecule possesses only sp^3 hybridized carbon atoms for which differences of CSA are generally very weak.[10] The detection of enantiodiscriminations on the basis of (one-bond) ^{1}H-^{13}C dipolar difference requests recording ^{1}H-^{13}C heteronuclear 2D experiments such as HETSERF or HSQC experiments.[16]

I.3 Experimental section

Material and general comments. The preparation of (sealed) anisotropic NMR tubes and practical aspects have been reported in previous papers.[2,4,5] However, two crucial points must be reminded. First it is preferable to directly weigh each component of the mixture within the NMR tubes and seal them to avoid organic solvent evaporation during NMR acquisitions. Second, it is necessary to avoid solute orientational inhomogeneities (mainly due to matter gradients) in order to obtain high-resolution

spectra. So far, several low-speed centrifugation cycles of the tube at short time repetition provide the best way to proceed (between each centrifugation cycle, the tube is inverted). Finally note that the solute can be extracted from the liquid crystals.

I.4 ^{31}P-^{31}P correlation 2D-NMR approaches

Figures SI-11a (top) and **SI-11b** report respectively the expansions of the anisotropic, proton-decoupled ^{31}P-^{31}P COSY spectrum (downfield diagonal) and T-resolved map (up-field region) of (±)-**16** showing ^{31}P signals of P_A and P_B atoms, respectively (the full spectra are shown in **Figure SI-5** and **SI-6**). Clearly the relative positions of diagonal and autocorrelation peaks on the COSY 2D map allow to unambiguously assign the signals for each enantiomer while the shifting of lines indicates that the spectral discrimination is mainly dominated by a difference of ^{31}P CSA ($\Delta\sigma$ = 4 Hz). The comparison with the 2D map of the enantioenriched mixture confirms this analysis (**Figure SI-11a, bottom)**. More interesting is the ^{31}P T-resolved spectrum presented in **Figure SI-11b** (see also **Figure SI-6**). Indeed, the separation of spectral information, $\delta(^{31}P)$ et T(^{31}P-^{31}P), on the F_2 and F_1 dimensions, respectively facilitates the analysis of lines and reveals clearly a tiny difference of total couplings ^{31}P-^{31}P (ΔT < 1 Hz) between the two enantiomers on both ^{31}P atom sites (P_A and P_B), thus confirming the measurement made on the 1D spectrum. Finally the last strategy to determine the ^{31}P enantio-resonances belonging to each isomer on spectrum of (*R*/*S*)-**16** consists in recording the ^{31}P-^{31}P INADEQUATE 2D experiment.[17] In this scheme, the double quantum (DQ) coherence of the two coupled ^{31}P atoms (an AX spin system) is excited and evolves during the t_1 dimension before being reconverted into single coherence(SQ) just before acquisition of the signal. After a double FT, the ^{31}P signal in F_1 is located at the sum of ^{31}P frequencies (measured in F_2) as seen in **Figure SI-11c**. As a direct consequence, the difference in Hz between the ^{31}P lines (DQ signal) observed in F_1 and associated to each enantiomer is doubled compared to the one measured in the F_2 dimension. Experimentally, a splitting of 8 Hz separates the two resonances, thus increasing the quality of the spectral enantiodiscrimination on the basis of $\Delta\sigma$□^{31}P). Theoretically, as the amplitude of the SQ → DQ transfer depends on the magnitude of coupling between interacting nuclei (here, T(^{31}P-^{31}P)), this experiment is basically less adapted for quantitative purposes, unlike previous experiments. However when the difference of total coupling for each enantiomer is less than 10-20%, the difference of signal amplitude remains moderate, thus giving the possibility to evaluate the *ee* with acceptable accuracy.

I.5 Assignment of ^{31}P atoms of chiral biaryl (16)

The assignment of ^{31}P atoms is not trivial. It derives from the combined spectral analysis of various NMR spectra: i)^{1}H 1D-NMR spectrum (with and without ^{31}P decoupling) (**Figure SI-17**); ii) ^{1}H-^{1}H COSY 2D map (**Figure SI-18**); iii) the ^{31}P J-resolved 2D map (**Figure SI-19**); and the iv) the ^{31}P-^{1}H HMBC 2D map (**Figure SI-20**). This latter shows the heteronuclear correlations between $^{31}P_A$ and H-3 atoms ($^3J(^{31}P_A$-$^1H_3)$ = 3.1 Hz) and between $^{31}P_B$ and H-9 atoms ($^3J(^{31}P_A$-$^1H_3)$ = 4.3 Hz (**Figure SI-13**). From the analysis of ^{1}H-^{1}H 2D COSY, the correlations ^{1}H-^{1}H (**Figure SI-18**) allow the assignment of the ^{1}H signals (3 and 4 correlations) of aromatic rings A and B. The result agrees with the analysis of ^{31}P J-resolved 2D map (**Figure SI-19**) that clearly shows the ^{1}H signals that are coupled (or not) with the phosphorous atoms $^{31}P_A$ and $^{31}P_B$.

I.6 References for ESI

1 J.W Emsley and J.C. Lindon in *NMR spectroscopy using liquid crystal solvents*, (1975). Pergamon Press, Oxford.

2 M. Sarfati, P. Lesot, D. Merlet and J. Courtieu, *Chem. Commun.*, 2000, 2069.

3 (*a*) C. Aroulanda, D. Merlet, J. Courtieu and P. Lesot, *J. Am. Chem. Soc.*, 2001, **123**, 12059; (*b*) P. Lesot, Z. Luz, C. Aroulanda and H. Zimmermann, *Magn. Reson. Chem.*, 2014, **52**, 581.

4 P. Lesot, C. Aroulanda, H. Zimmerman and Z. Luz, *Chem. Soc. Rev.*, 2015, **44**, 2330.

5 (*a*) C. Aroulanda, M. Sarfati, J. Courtieu and P. Lesot, *Enantiomer*, 2001, **6**, 281; (*b*) C. M. Thiele, S. Berger, *Org. Lett.* 2003, **5**, 705; (*c*) P. Lesot, O. Lafon, C. Aroulanda and R. Dong, *Chem. Eur. J.,* 2008, **14***,* 4082.

6 (*a*) O. Lafon, P. Lesot, M. Rivard, M. Chavarot, F. Rose-Munch and E. Rose, *Organometallics*, 2005, **24**, 4021; (*b*) M. Sarfati, C. Aroulanda, J. Courtieu and P. Lesot, *Tetrahedron: Asymmetry*, 2001, **12**, 737.
7 (*a*) A. Meddour, I. Canet and J. Courtieu, *J. Am. Chem. Soc*., 1994, **116**, 9652; (*b*) I. Canet, J. Courtieu, A. Meddour, A. Loewenstein and J.-M. Péchiné *J. Am. Chem. Soc*., 1995, **117**, 6520.
8 (*a*) M. Jacubova A. Meddour, J.-M. Péchiné, A. Baklouti and J. Courtieu, *J. Fluorine Chem.,* 1977, **89**, 149; (*b*) V. Madiot, P. Lesot, D. Grée, J. Courtieu and R. Grée, *Chem. Commun.*, 2000, 169.
9 A. Meddour, J. Uziel, J. Courtieu and S. Jugé, *Tetrahedron: Asymmetry*, 2006, **17**, 1424.
10 (*a*) A. Meddour, P. Berdagué, A. Hedli, J. Courtieu and P. Lesot *J. Am. Chem. Soc*., 1997, **119**, 4502; (*b*) P. Lesot, O. Lafon, J. Courtieu and P. Berdagué**,** *Chem. Eur. J.,* 2004, **10**, 3741; (*c*) P. Tzvetkova, B. Luy and S. Simova, *Topics in Chemistry and Material Science* 5 (2011) pp. 70-77 of Current Issues in Organic Chemistry, (Eds: R. D. Nikolova, S. Simova, P. Denkova, G. N. Vayssilov), Heron Press Ltd, Birmingham, 2011.
11 (*a*) P. Lesot, D. Merlet, A. Loewenstein and J. Courtieu, *Tetrahedron: Asymmetry*, 1998, **9**, 1871; (*b*) D. Merlet, B. Ancian, J. Courtieu and P. Lesot, *J. Am. Chem. Soc.*, 1999, **121**, 5249; (*c*) P. Lesot, M. Sarfati and J. Courtieu *Chem. Eur. J.*, 2003, **9**, 1724; (*d*) O. Lafon, P. Lesot, D. Merlet and J. Courtieu, *J. Magn. Reson.,* 2004, **171**, 135; (*e*) P. Lesot in *Deuterium NMR of Liquid-Crystalline Samples at Natural Abundan*ce, *Encyclopedia of Magnetic Resonance (eMagRes)*, 2013, **2 (3)**, 315, Doi:10.1002/9780470034590.Emrstm1318.
12 J. Farjon, D. Merlet, P. Lesot and J. Courtieu, *J. Magn. Reson.*, 2002, **158**, 169.
13 D. Merlet, L. Béguin, J. Courtieu and N. Giraud, *J. Magn. Reson.*, 2011, **209**, 315.
14 P. Lesot and O. Lafon, *Anal. Chem.,* 2012, **84**, 4569.
15 (*a*) D. Merlet, B. Ancian, J. Courtieu and P. Lesot, *J. Am. Chem. Soc.*, 1999, **121**, 5249; (b) O. Lafon, P. Lesot, D. Merlet and J. Courtieu, *J. Magn. Reson.,* 2004, **171**, 135.
16 (*a*) J. Farjon, J.-P. Baltaze, P. Lesot, D. Merlet and J. Courtieu, *Magn. Res. Chem.*, 2004, **42**, 594, (2004); (*b*) S. Chaudhari, N. Nilamoni and N. Suryaprakash, *RSC Advances*, 2012, **2**, 12915; (*c*) N. Lokesh and N. Suryaprakash, *Chem. Phys. Lett.* 2015*,* **625**, 10.
17 (*a*) A. Bax, R. Freeman and S. P. Kempsell, *J. Am.Chem.Soc*. 1980, **102**, 4849; (*b*) A. Bax, R. Freeman and S. P. Kempsell, *J. Magn. Reson*. 1980, **41**, 349; (*c*) A. Bax, R. Freeman, T. A. Frenkiel and M. H. Levitt, *J. Magn. Reson*. 1981, **43**, 478; (*d*) A. Bax and R. Freeman, *J. Magn. Reson*. 1980, **4**1, 507; (*e*) P. Lesot, J. W. Emsley and J. Courtieu; *Liq. Crystals*, 1998, **25**, 123.

II. Supplementary Tables

Table SI-1: Notation, formula and sample compositions of 19 samples (17 solutes) ranked by Series (**I** to **IV**) and increasing number of Carbon and Hydrogen nuclei[a]

Series	Solute Nb	Formula	Mw (g/mol)	m(Solute) (mg)	m(PBLG) (mg)	m(Co-solvent) (mg)	% w/w PBLG
I	**1**	$C_{12}H_7IBr_2$	437.9	19.9	90.3	531.6 (C**D**Cl_3)	14.1
	2	$C_{13}H_8O_2Br_2$	356.0	54.5	92.6	520.5 ($CHCl_3$)	13.9
	3	$C_{13}H_8OBr_2$	340.0	61.1	96.5	537.3 ($CHCl_3$)	13.9
	4	$C_{13}H_{10}OBr_2$	342.0	100	92.4	471.3 ($CHCl_3$)	14.0
	5	$C_{13}H_{10}Br_2$	326.0	21.2	90.1	532.1 (C**D**Cl_3)	14.0
	6	$C_{14}H_{10}O_2Br_2$	370.0	72.2	90.6	487.6 ($CHCl_3$)	13.9
II	**7**	$C_{12}H_7IBrCl$	393.4	21.0	90.1	532 (C**D**Cl_3)	14.0
	8	$C_{13}H_8O_2BrCl$	311.6	59.5	91.0	503.1 (C**D**Cl_3)	13.9
	9	$C_{13}H_8OBrCl$	295.6	62.6	92.5	512.5 ($CHCl_3$)	13.9
	10			19.0	90.7	541.3 (C**D**Cl_3)	14.0
	10' (*R*)	$C_{13}H_{10}BrCl$	281.6	19.5 (*R*)	90.6	537.7 (C**D**Cl_3)	14.0
	11	$C_{14}H_{10}O_2BrCl$	325.6	70.1	90.9	488.2 ($CHCl_3$)	14.0
III	**12**	$C_{24}H_{17}PBrCl$	451.7	26.0	91.9	539.2 ($CDCl_3$)	14.0
	13	$C_{24}H_{17}P(O)BrCl$	467.7	96.2	101.7	537.5 ($CHCl_3$)	13.8
	14	$C_{24}H_{29}PBrCl$	463.8	25.3	96.4	570.0 ($CHCl_3$)	13.9
	15	$C_{24}H_{29}P(O)BrCl$	479.8	20.1	96,2	579.8 ($CHCl_3$)	13.8
IV	**16**	$C_{36}H_{27}P_2Cl$	557.0	30.4	92.3	545.6 (C**D**Cl_3)	13.9
	16' (*R*)			15.4 (±)+16.2 (*R*)	92.1	538.7 (C**D**Cl_3)	13.9
	17	$C_{14}H_{13}OBr$	277.2	100.6	91.1	460.5 ($CHCl_3$)	14.0

[a]Major enantiomer in enantioenriched samples is indicated in column 2. [b]The error on weighing is ± 0.5 mg.

Table SI-2: Number of ^{31}P, ^{13}C and ^{2}H sites experimentally discriminated and the largest spectral enantiodifference ($|\Delta\Delta\sigma|$ or $|\Delta\nu_Q|$) measured on spectra recorded in PBLG/chloroform

Comp. (Series)	Formula Mw (g/mol)	Nb. of ^{31}P sites ($|\Delta\Delta\sigma|^{max}$ in Hz)[a]	Nb. of ^{13}C sites ($|\Delta\Delta\sigma|^{max}$ in Hz)[a]	Nb. of ^{2}H sites ($|\Delta\Delta\nu_Q|^{max}$ in Hz)[b]
1 (I)	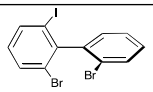 $C_{12}H_7IBr_2$ 437.9	-	1 / 12 $|\Delta\Delta\sigma|$ = 2	-
2 (I)	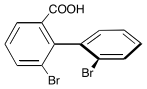 $C_{13}H_8O_2Br$ 356.0	-	12 / 13 $|\Delta\Delta\sigma|$ = 14	Unexploitable results
3 (I)	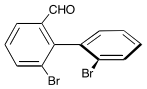 $C_{13}H_8OBr_2$ 340.0	-	9 / 13 $|\Delta\Delta\sigma|$ = 3.5	7* / 8 $|\Delta\Delta\nu_Q|$ = 66
4 (I)	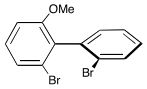 $C_{13}H_{10}OBr_2$ 342.0	-	10 / 13 $|\Delta\Delta\sigma|$ = 2.5	7* / 8 $|\Delta\Delta\nu_Q|$ = 125
5 (I)	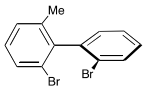 $C_{13}H_{10}Br_2$ 326.0	-	6 / 13 $|\Delta\Delta\sigma|$ = 2.5	-
6 (I)	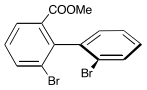 $C_{14}H_{10}O_2Br_2$ 370.0	-	8 / 13 $|\Delta\Delta\sigma|$ = 4.5	5 / 8 $|\Delta\Delta\nu_Q|$ = 152
7 (II)	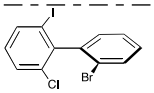 $C_{12}H_7IBrCl$ 393.4	-	3 / 12 $|\Delta\Delta\sigma|$ = 2.5	-
8 (II)	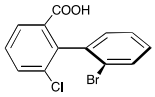 $C_{13}H_8O_2BrCl$ 311.6	-	11 / 13 $|\Delta\Delta\sigma|$ = 14	Unexploitable results
9 (II)	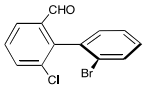 $C_{13}H_8OBrCl$ 295.6	-	11 / 13 $|\Delta\Delta\sigma|$ = 3.5	6 / 8 $|\Delta\Delta\nu_Q|$ = 78
10 (II)	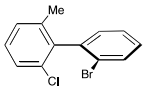 $C_{13}H_{10}BrCl$ 281.6	-	6 / 13 $|\Delta\Delta\sigma|$ = 3.5	-

Table SI-2 (continued):

Comp. (Series)	Formula Mw (g/mol)	Nb. of ^{31}P sites ($\|\Delta\Delta\sigma\|^{max}$ in Hz)[a]	Nb. of ^{13}C sites ($\|\Delta\Delta\sigma\|^{max}$ in Hz)[a]	Nb. of ^{2}H sites ($\|\Delta\Delta\nu_Q\|^{max}$ in Hz)[b]
11 (II)	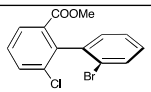 $C_{14}H_{10}O_2Br$ 325.6	-	8 / 13 $\|\Delta\Delta\sigma\|$ = 4.5	5 / 8 $\|\Delta\Delta\nu_Q\|$ = 149
12 (III)	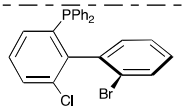 $C_{24}H_{17}PBrCl$ 451.7	0 / 1	4 / 24 $\|\Delta\Delta\sigma\|$ = 3	-
13 (III)	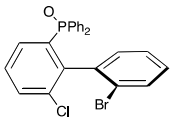 $C_{24}H_{17}OPBrCl$ 467.7	0 / 1	12 / 24 $\|\Delta\Delta\sigma\|$ = 7.5	-
14 (III)	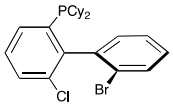 $C_{24}H_{29}PBrCl$ 463.8	1 / 1 $\|\Delta\Delta\sigma\|$ = 6.8	3 / 24 $\|\Delta\Delta\sigma\|$ = 4	-
15 (III)	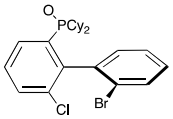 $C_{24}H_{29}OPBrCl$ 479.8	0 / 1	2 / 24 $\|\Delta\Delta\sigma\|$ = 2.5	-
16 (IV)	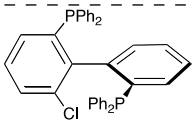 $C_{24}H_{17}PBrCl$ 557.0	2 / 2 $\|\Delta\Delta\sigma\|$ = 4.5	12 / 36 $\|\Delta\Delta\sigma\|$ = 9.5	-
17 (IV)	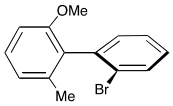 $C_{14}H_{13}OBr$ 277.2	-	6 / 14 $\|\Delta\Delta\sigma\|$ = 1.5	7 / 9 $\|\Delta\Delta\nu_Q\|$ = 85

[a] Largest enantiodifference of CSA : $|\Delta\Delta\sigma|^{max} = |\Delta\sigma(R) - \Delta\sigma(S)|$

[b] Largest enantiodifference of RQC : $|\Delta\Delta\nu_Q|^{max} = |\Delta\nu_Q(R) - \Delta\nu_Q(S)|$

Table SI-3: $\delta(^{13}C)$ (in ppm) and spectral discrimination between enantiomers for each ^{13}C site (in Hz) observed at 298 K

Solute (Series)	Formula	Nb. of ^{13}C sites discriminated	$\delta(^{13}C)$ and $\Delta\Delta\sigma(^{13}C)^{a,b,c,}$
1 (I)	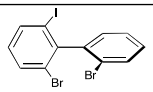	1 / 12	**145.65** (0), **145.00** (0), 138.01 (0), 132.55 (0), 132.54 (0), 130.68 (0), 130.43 (0), 129.73 (0), 127.41 (0), **123.19** (0), **123.12** (0), **100.10** (2)
2 (I)	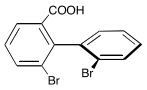	12 / 13	**168.75** (0), **142.13** (2.5), **141.96** (5), 136.07 (9), 132.91 (14), 130.91 (12), **130.17** (6), 130.14 (4), 128.92 (6.5), 128.84 (4.5). 127.89 (5.5), **124.87** (11), **123.62** (9.5)
3 (I)	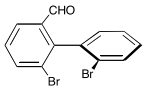	9 / 13	190.40 (0), **144.39** (2.5), 137.81 (0), **136.95** (0), **135.69** (1.5), 132.19 (1.5), 130.89 (2.5), 129.67 (0), 129.61 (2), 126.84 (2), 126.40 (3,5), **125.28** (3), **123.38** (1)
4 (I)	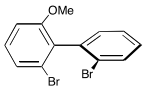	10 / 13	**157.74** (1.5), **138.45** (2), 131.92 (0), 131.00 (0), **130.92** (1), 129.80 (2), 128.78 (2), 126.68 (1), 124.38 (2.5), **124.31** (1.5), **123.85** (0), 109.71 (1.5), 55.73 (2)
5 (I)	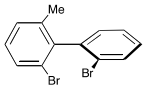	6 / 13	**141.56** (2.5), **141.50** (2.5), **138.74** (2), 132.56 (0), 130.47 (0), 130.01 (1), 129.24 (2.5), 129.14 (2.5), 128.88 (0), 127.40 (0), **124.00** (0), **123.45** (0), 20.88 (0)
6 (I)	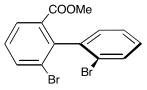 $C_{14}H_{10}O_2Br_2$	8 / 13	**165.80** (0), **141.89** (2), **140.73** (0), 136.15 (0), **132,13** (1,5), 131,55 (4), 129.52 (4.5), 129.14 (2.5), 128.96 (3), 128.59 (0), 126.35 (0), **125.51** (3.5), **122.70** (1,5), 51.83 (0)
7 (II)	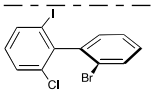	3 / 12	**144.07** (0), **143.20** (0), 137.46 (0), **133.53** (1), 132.58 (0), 130.55 (0), 130.41 (0), 129.76 (0), 129.32 (1), 127.42 (0), **123.31** (0), **100.49** (2.5),
8 (II)	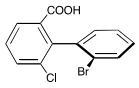 I	11 / 13	**169.18** (0), **140.34** (0), **139.84** (5.5), **134.42** (11.5), 132.98 (7.5), 132.74 (14), 130.71 (12), **130.19** (5.5), 129.94 (5), 128.62 (4), 128.45 (7.5), 127.68 (4). **123.51** (7.5)
9 (II)	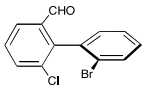	11 / 13	190.17 (1), **142.43** (2), **135.46** (1.5), **135.17** (0), **134.80** (2.5), 134.61 (1.5), 132.19 (3.5), 130.96 (3), 129.68 (0), 129.33 (2), 126.82 (1.5), 125.82 (3), **123.49** (0.5)
10 (II)	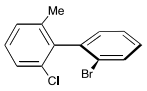	6 / 13	**139.75** (2.5), **139.62** (2.5), **138.63** (1.5), **133.61** (0), 132.58 (0), 130.56 (0), 129.17 (3.5), 128.91 (3.5), 128.25 (0), 127.40 (1.5), 126.79 (0), **123.60** (0), 20.49 (0)

Table SI-3 (continued):

Solute (Series)	Formula	Nb. of ^{13}C sites discriminated	$\delta(^{13}C)$ and $\Delta\Delta\sigma(^{13}C)$[a,b,c,]
11 (III)	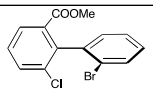	8 / 13	**165.88** (0), **140,08** (2.0), **138,92** (0.5), **134,94** (3.5), 132.92 (0), **132,05** (1,5), 131,58 (4), 129,55 (4.5), 128.74 (0), 128,61 (0), 128,53 (3.5), 126,37 (0), 122.77 (2), 51,80 (0)
12 (IV)	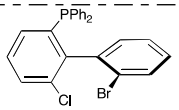	4 / 24[d]	144.71 (0), 140.10 (0), 138.81 (0), 136.52 (0) 135.54 (0), 134.53 (0), 133.74 (0), 133.57 (3) 132.24 (0), 132.18 (0), 132.08 (0), 131.52 (0) 129.81 (0), 129.11 (0), 129.04 (2), 128.73 (0) 128.69 (0), 128.45 (0), 128.38 (3), 128.11 (0) 127.43 (0), 126.91 (0), 126.28 (0), 123.94 (2)
13 (IV)	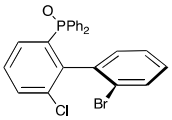	12 / 24[d]	**142.75** (7,5). **136.22** (0). **136.19** (0), **134.04** (5,5) 132.63 (5,5), **132.27** (0). 131.82 (2), 131.72 (0) **131.64** (0), 131.43 (2,5), 131.26 (3), 131.17 (0) 130.80 (4), 130.63 (0), 128.79 (2,5), 128.17 (7) 127.85 (2), 127.51 (0), 125.53 (2,5), 124.40 (3).
14 (IV)	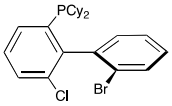	3 / 24[d]	**146.19** (0), **139.54** (0), **134.62** (0), 132.10 (4) 131.88 (0), 130.17 (3,5), 129.25 (0), 128.25 (0) 126.27 (3), 126.15 (0), **124.58** (0), **123.86** (0) 34.92 (0), 33.44 (0), 30.34 (0), 29.70 (0) 29.50 (0), 28.87 (0), 27.0 (0)[e], 26.78 (0) 26.73 (0), 25.9 (0)[e]
15 (IV)	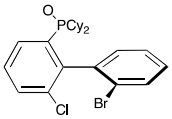	2 / 24[d]	**141.79** (0), **138.43** (0), **136.07** (0), **130.00** (0), 132.15 (2.5), 131.83 (0), 130.90 (0), 130.25 (2), 129.30 (0), 128.24 (0), 126.31 (0), **124.61** (0), 37.64 (0), 37.22 (0), 26.35 (0), 26.15 (0), 26.11 (0), 25.97 (0), 25.91 (0), 25.73 (0), 25.45 (0), 25.38 (0)
16 (V)	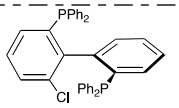	12 / 36[d]	**144.86** (9.5), **144.27** (7.5), **140.45** (6), 138.26 (0), **137.76** (3), **136.76** (0), 136.55 (0), **136.36** (4.5), **135.02** (3), 134.69 (0), 133.88 (0), 133.76 (0), 133.56 (5.5), 133.22 (0), 132.16 (7), 130.74 (0), 129.38 (4), 128.71 (5), 126.61 (5), 128.37 (0), 128.31 (0), 128.28 (0)[f], 128.04 (0), 127.95 (0), 127.71 (7.5)

Table SI-3 (continued):

Solute (Series)	Formula	Nb. of ^{13}C sites discriminated	$\delta(^{13}C)$ and $\Delta\Delta\sigma(^{13}C)$[a,b,c,]
17 (V)	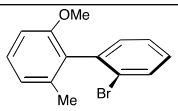	6 / 14	**156.55** (0), **138.63** (0), **137.38** (1.5), 132.01 (1), 130.89 (1.5), **129.81** (0), 128.47 (0), 128.19 (0), 126.77 (0), **124.15** (1.5), 122.00 (1), 108.15 (1.5), 55.37 (0), 19.53 (0)

[a] The ^{13}C signal of $CHCl_3$in the CLC is calibrated at 77 ppm.
[b] In parenthesis is given the separation between ^{13}C lines (in Hz) for a given site.
[c] The δ of quaternary carbons are written in bold.
[d] The $\delta(^{13}C)$ of resonances listed here was achieved from the analysis of ^{13}C-{^{1}H} and ^{13}C-{^{1}H, ^{31}P} 1D-NMR spectra and ^{13}C-{^{1}H} and ^{13}C-{^{1}H, ^{31}P} J-mod 1D-NMR spectra.
[e] An unresolved structure containing two resonances is observed on the ^{13}C-{^{1}H, ^{31}P} 1D-NMR spectrum.
[f] Intense and broad structure containing seven peaks on the ^{13}C-{^{1}H, ^{31}P} 1D-NMR spectrum.

Table SI-4: Values of lowest-energy conformer (a.u.), values of biaryls interplanar torsional angle (degree), values of scalar and x, y, z components of molecular electric dipole moment (debye), and map of electrostatic potential surface determined by the means of the continuous polarization model and using $CHCl_3$ as implicit solvent[a]

Solute (Series) **Energy[b]** **Angle[c]**	**μ_{mol} (scalar)** **[μ_x, μ_y, μ_y] [d]**	**Axes of μ_{mol}**	**Topologies[e] (EPS)**	**Nb. of ^{13}C and ^{2}H sites discriminated**
1 (I) 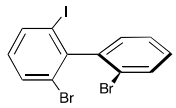 E = **−499.29** ϕ = **+88.63°**	**2.132** +0.626 +1.004 -1.773	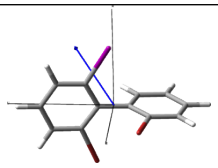	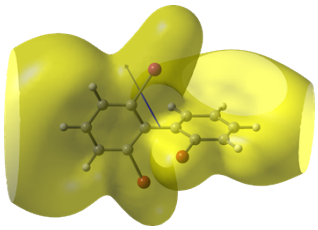	1 / 12 -
2 (I) 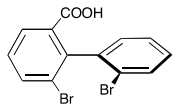 E = **−677.15** ϕ = **+93.24°**	**2.529** +0.006 -0.689 -2.433	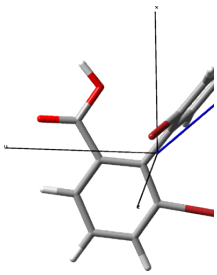	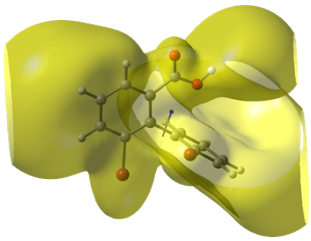	12 / 13 unexploitable NAD spectrum
3 (I) 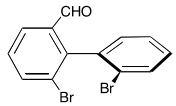 E = **−601.87** ϕ = **91.03 °**	**2.933** +0.026 -2.392 +1.696	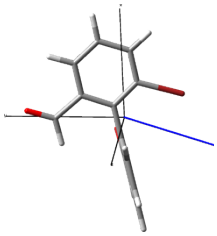	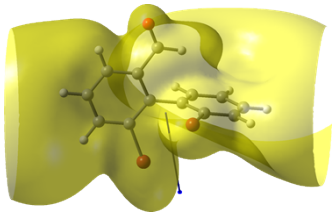	9 / 13 7 / 8
4 (I) 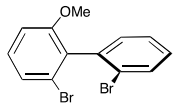 E = **−603.08** ϕ = **+93.65°**	**4.213** +0.268 +3.438 +2.420	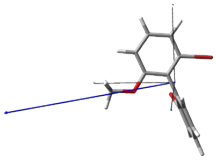	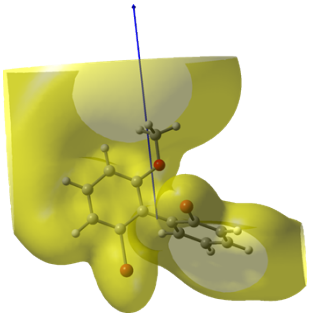	10 / 13 7 / 8
5 (I) 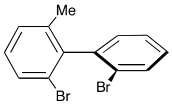 E = **−527.85** ϕ = **+92.32°**	**3.104** -0.391 +1.226 +2.825	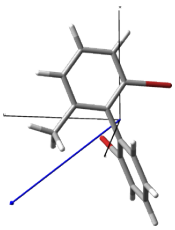	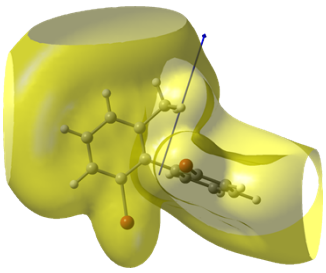	6 / 13 -

Table SI-4 (continued):

Solute (Series) Energy[b] Angle[c]	μ_{mol} (scalar) [μ_x, μ_y, μ_y] [d]	Axes of μ_{mol}	Topologies[e] (EPS)	Nb. of discriminated ^{13}C and ^{2}H sites
6 (I) 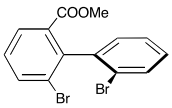 **E = -716.46** **ϕ = +94.11°**	**2.963** +0.452 -0.912 -2.783	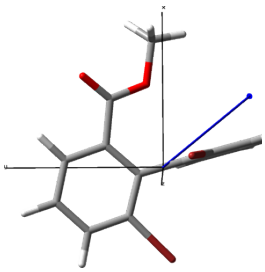	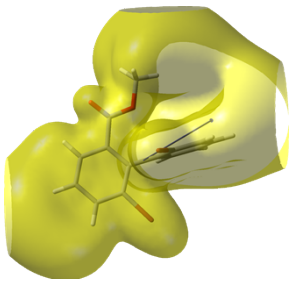	8 / 13 6 / 8
7 (II) 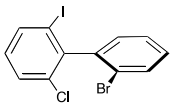 **E = -501.08** **ϕ = +87.62°**	**2.213** +1.348 +0.442 -1.698	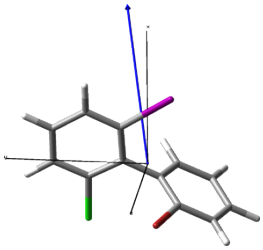	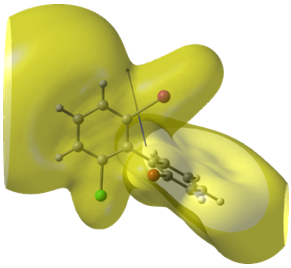	3 / 12 -
8 (II) 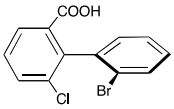 **E = -678.94** **ϕ = +91.21°**	**2.357** -0.333 +0.071 -2.3324	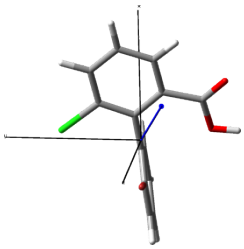	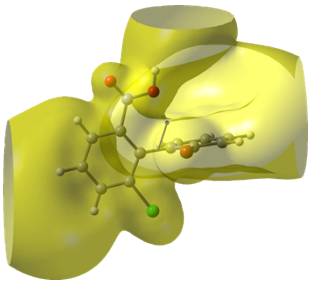	11 / 13 unexploitable NAD spectrum
9 (II) 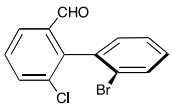 **E = -603.66** **ϕ = 89.73°**	**2.737** -0.491 +2.051 -1.745	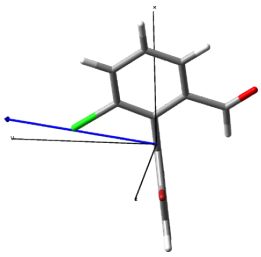	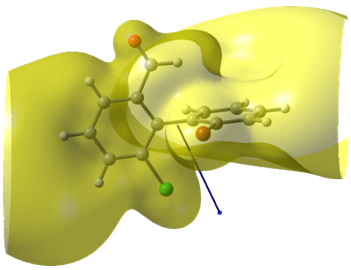	11 / 13 6 / 8
10 (II) 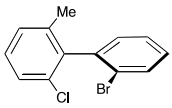 **E = -529.64** **ϕ = +92.42°**	**3.179** -0.098 +0.510 +3.136	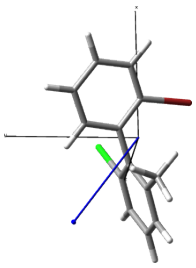	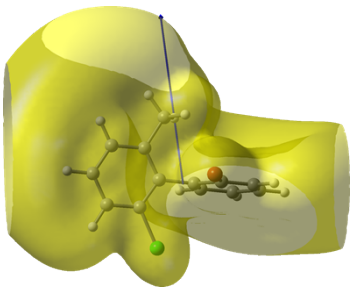	6 / 13 -

Table SI-4 (continued):

Solute (Series) Energy[b] Angle[c]	μ_{mol} (scalar) [μ_x, μ_y, μ_y] [d]	Axes of μ_{mol}	Topologies[e] (EPS)	Nb. of discriminated ^{13}C and ^{2}H sites
11 (II) 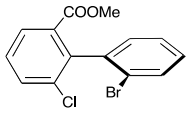 **E = -718.25** **ϕ = +94.52°**	**3.006** +0.9541 +0.4669 -2.8118	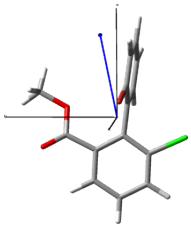	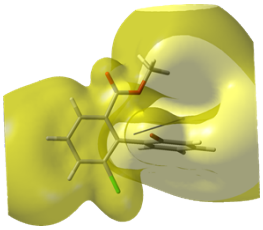	8 / 13 6 / 8
12 (III) 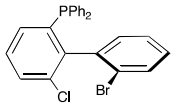 **E = -1294.49** **ϕ = +89.69°**	**4.166** +3.515 +1.854 +1.249	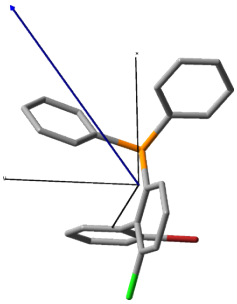	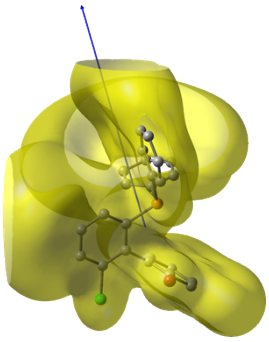	4 / 24 -
13 (III) 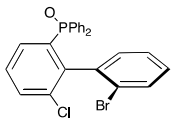 **E = -1369.76** **ϕ = +77.79°**	**4.622** +2.904 +0.605 -3.545	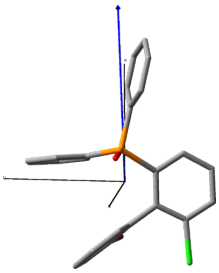	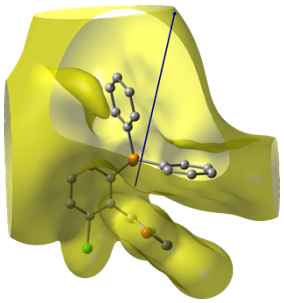	12 / 24 -
14(III) 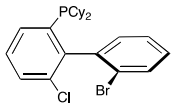 **E = -1301.74** **ϕ = 82.80°**	**3.048** +2.241 -0.163 +2.059	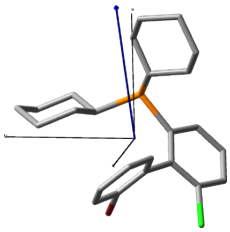	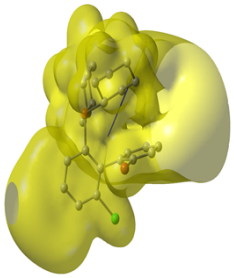	3 / 24 -
15 (III) 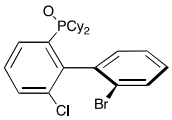 **E = -1377.03** **ϕ = +82.73°**	**5.146** +0.386 -0.020 +5.131	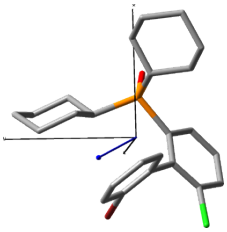	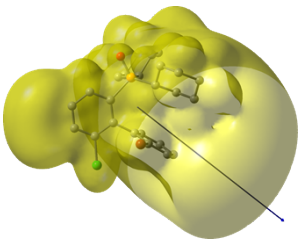	2 / 24 -

Table SI-4 (continued):

Solute (Series) Energy[b] Angle[c]	μ_{mol} (scalar) [μ_x, μ_y, μ_y] [d]	Axes of μ_{mol}	Topologies[e] (EPS)	Nb. of discriminated ^{13}C and ^{2}H sites
16 (IV) 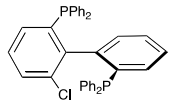 **E = -2086.11** **ϕ = +81.97°**	**5.290** -4.220 +3.023 +1.021	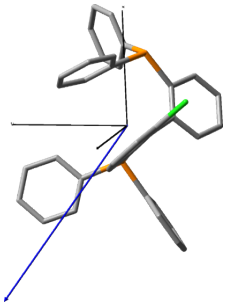	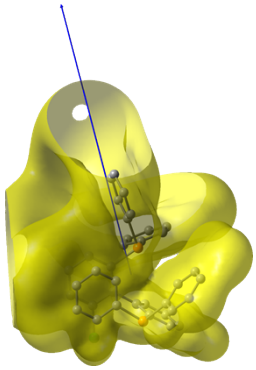	12 / 36 -
17 (IV) 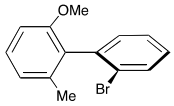 **E = -629.85** **ϕ = +88.28°**	**2.377** +0.696 +2.225 +0.465	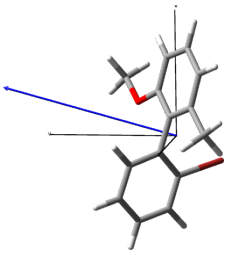	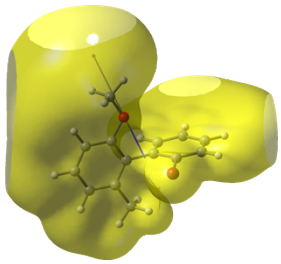	6 / 14 7 / 9

[a]Geometry optimizations and electronic structure determinations were carried out using the Gaussian 09 program (see Experimental Section in the article for details and references).
[b]Value of energy (a.u.) of more stable conformer.
[c]Value of the biaryl interplanar angle (degree). As depicted below, the sign of the aforementioned interplanar angle was arbitrarily chosen for all biaryls by measuring the sign of $\phi_{X\text{-}C\text{-}Z}$, where positions X, C and Z are highlighted in red in the figure shown below.
Required parameters are missing or incorrect.
[d]Values of scalar and x, y, z components of tmolecular electric dipole moment (debye).
[e]Electrostatic Potential Surfaces maps were plotted by using the same contour level for all species (isovalue = 0.005 a.u.) in order to correlate species with families of a given topology: cylindrical and spherical topologies were assigned for series {I, II, IV(17)} and {III, IV(16)}, respectively.

III. Supplementary figures

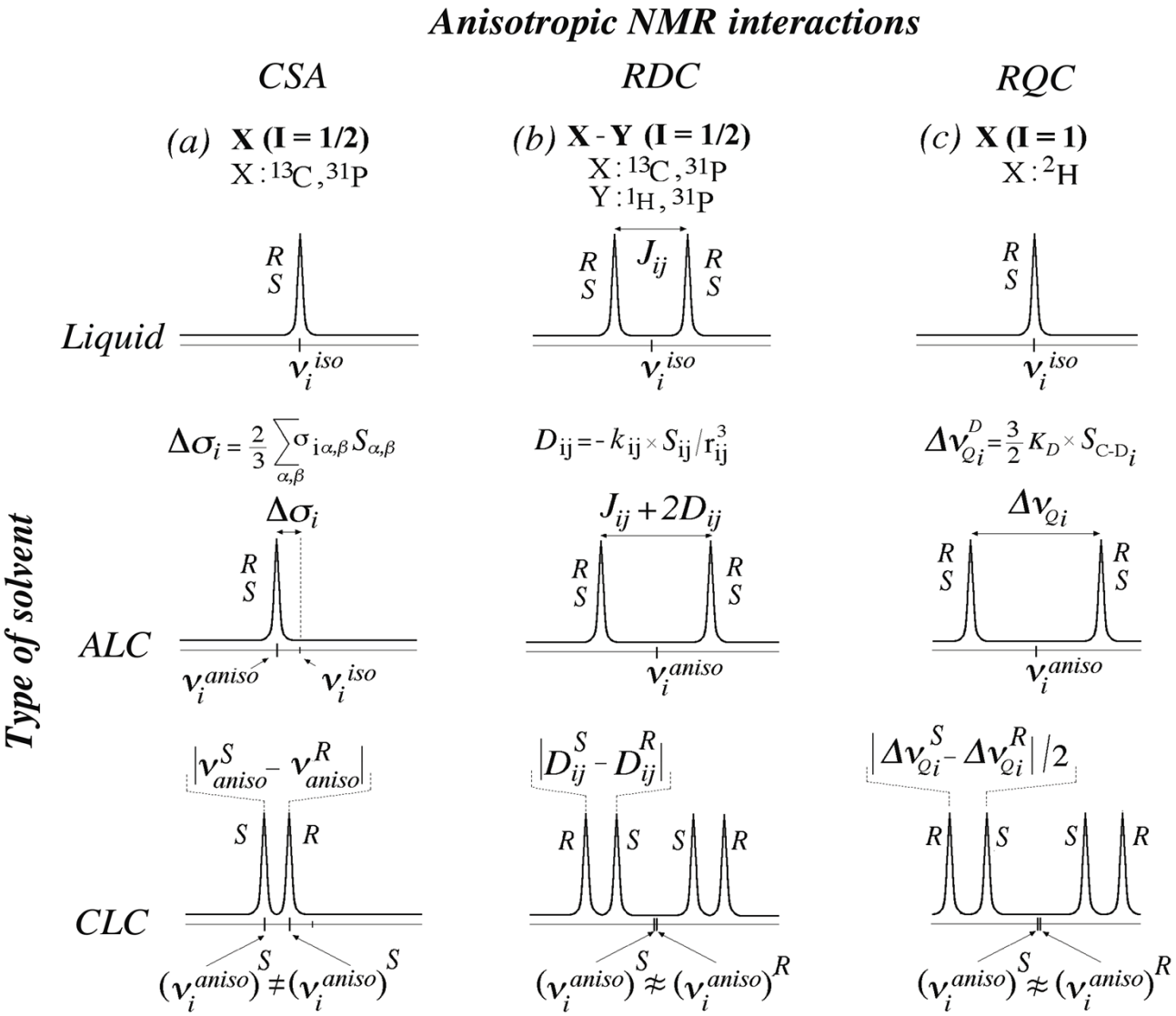

Fig. SI-1. Schematic principle of the ^{13}C, ^{31}P and ^{2}H spectral enantiodiscriminations in CLC based on a difference of (a) chemical shift anisotropies (CSA), □□, (b) residual dipolar couplings (RDC), D_{ij}, and (c) residual quadrupolar couplings (RQC), $\Delta\nu_Q$. For simplicity, we have considered that $\nu_i^{iso} = \nu_i^{aniso}$ (no CSA and solvent effect) for spectral patterns associated to RDC and RQC. In formula, $S_{\alpha\beta}$□and S_{ij} are molecular and internuclear order parameters, respectively, while k_{ij} and K_D are the dipolar ($k_{ij} = h\gamma_i\gamma_j/4\pi^2$) and quadrupolar coupling constant ($K_D = e^2Q_Dq_{C\text{-}D}/h$), respectively. For a and c, a single nucleus is considered (isolated spin or proton decoupled signals). The *R*/*S* assignments shown in all spectra are arbitrarily defined. The intensities of signals are not plotted to scale.

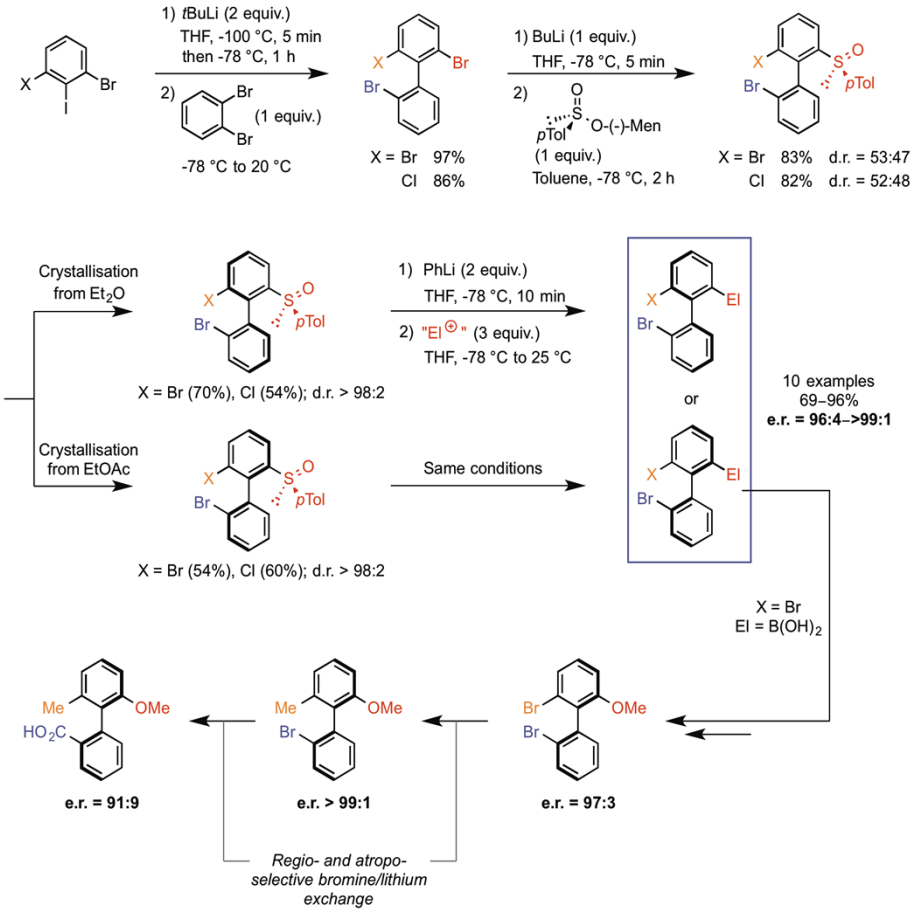

Fig. SI-2. Schematic pathway leading to the preparation of the chiral *ortho*-trisubstituted biaryls **2**, **5** and **17**. Details on the synthesis of other biaryls can be found in refs. 8, 18 and 19 of the article.

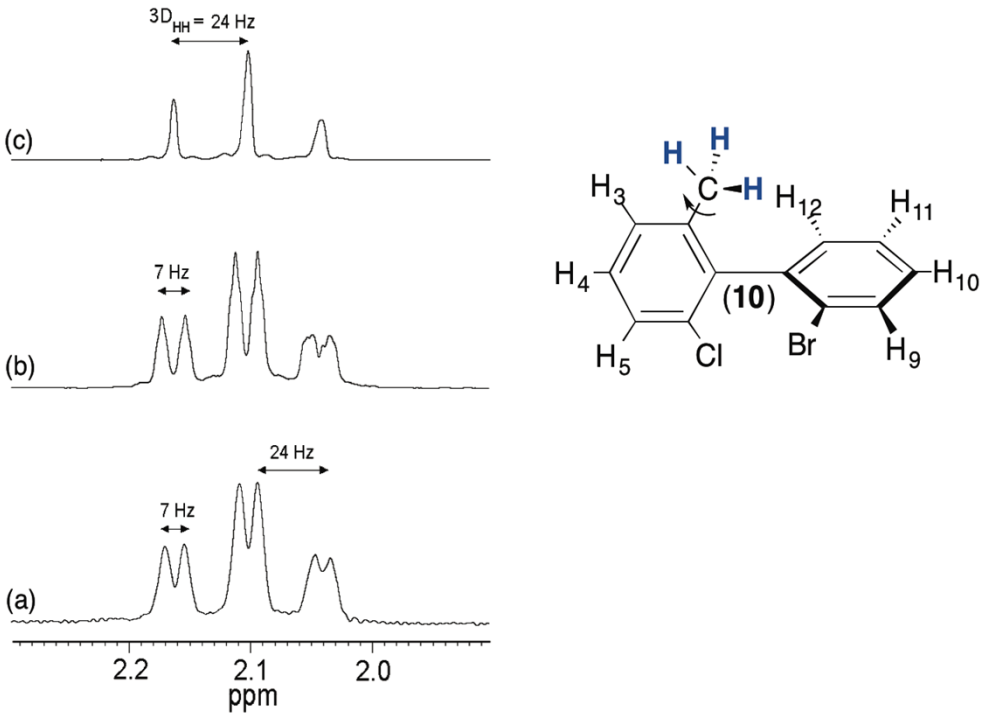

Fig. SI-3. 400.1 MHz ^{1}H signal (2.1 ppm) of methyl group of (a) (*R*/*S*)-**10** and (b) (*R*)-**10** both dissolved in the chiral mesophase, PBLG/$CHCl_3$. (c) Same spectrum as (b) when aromatic signals located at 7.23 ppm (H-3) are selectively irradiated (homodecoupling). Note the absence of doubling in (c).

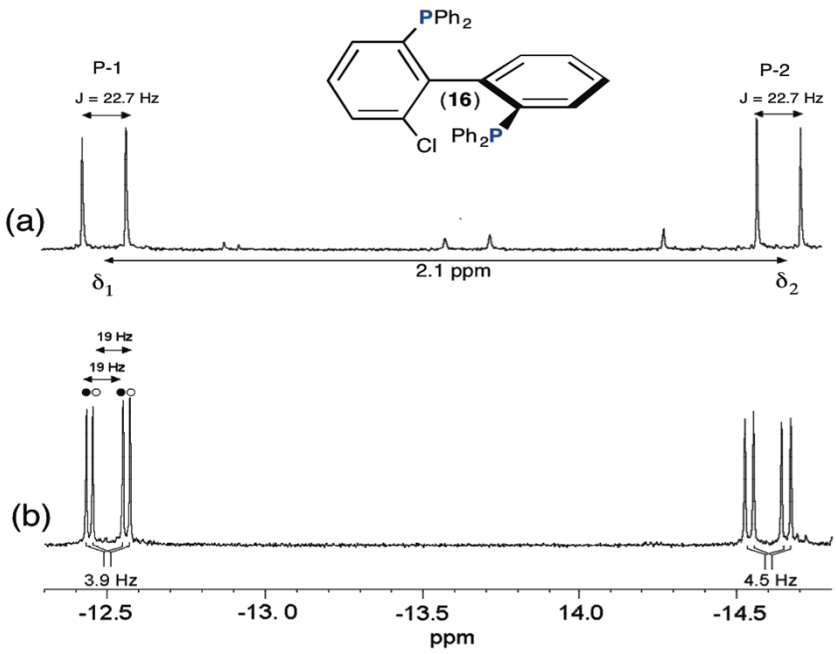

Fig. SI-4. 161.9 MHz ^{31}P-{^{1}H} 1D-NMR spectrum of (±)-**16** dissolved in (a) achiral isotropic solvent ($CHCl_3$) and (b) in PBLG/$CHCl_3$. Note the doubling of ^{31}P signals originating from the spectral enantiodiscrimination of (±)-**16** in the CLC.

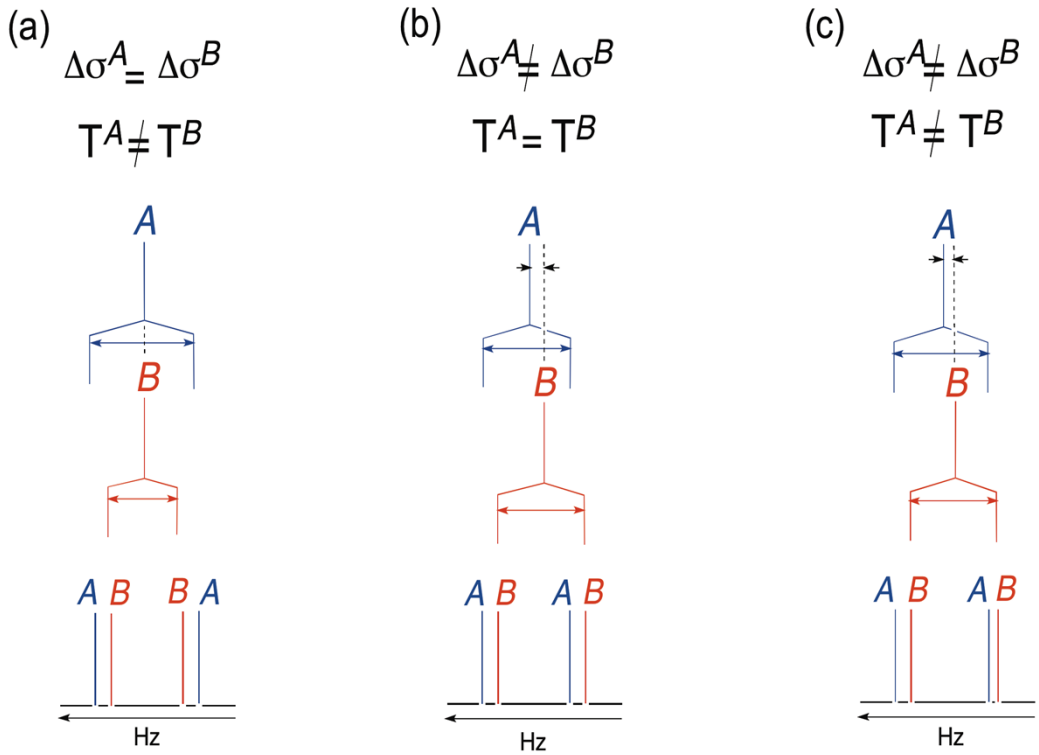

Fig. SI-5. Three possible spectral solutions explaining the presence of two doublets for P1 of (*R/S*)-**16** based on: (a) a difference of T(^{31}P-^{31}P) but not Δσ(^{31}P), (b) a difference of Δσ(^{31}P) but not T(^{31}P-^{31}P), (c) on a difference of T(^{31}P-^{31}P) and Δσ(^{31}P). Note that splittings between *A*/*B* lines (shielded components) differ in the (c) situation (contrarily to the a and b cases).

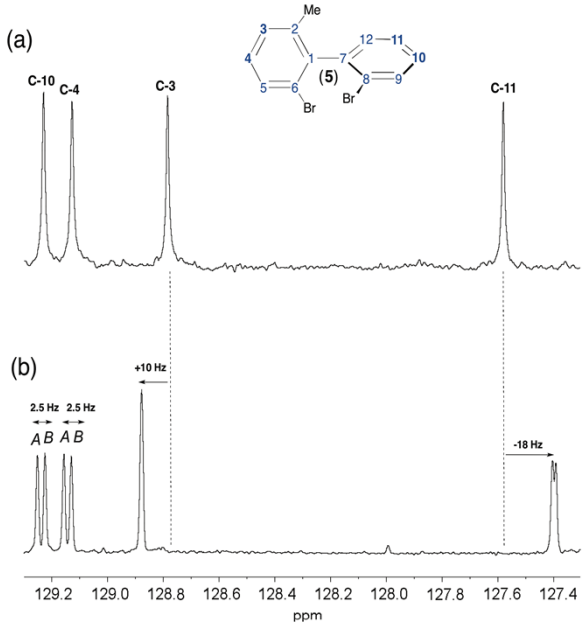

Fig. SI-6. Example of comparison between the 100.4 MHz ^{13}C-{^{1}H} 1D-NMR spectrum (region between 127.2 and 129.4 ppm) of (*R/S*)-**5** recorded in (a) isotropic solution ($CHCl_3$) and in CLC (PBLG/$CHCl_3$). Note the shift of ^{13}C resonances (up to 18 Hz) due to both the ^{13}C CSA anisotropy (due to the ordering) and the solvent effect. In both spectra, the ^{13}C signal of $CHCl_3$ has been arbitrarily calibrated at 77 ppm. On this region, largest enantiodiscriminations are observed on C-10 and C-4 carbon atoms.

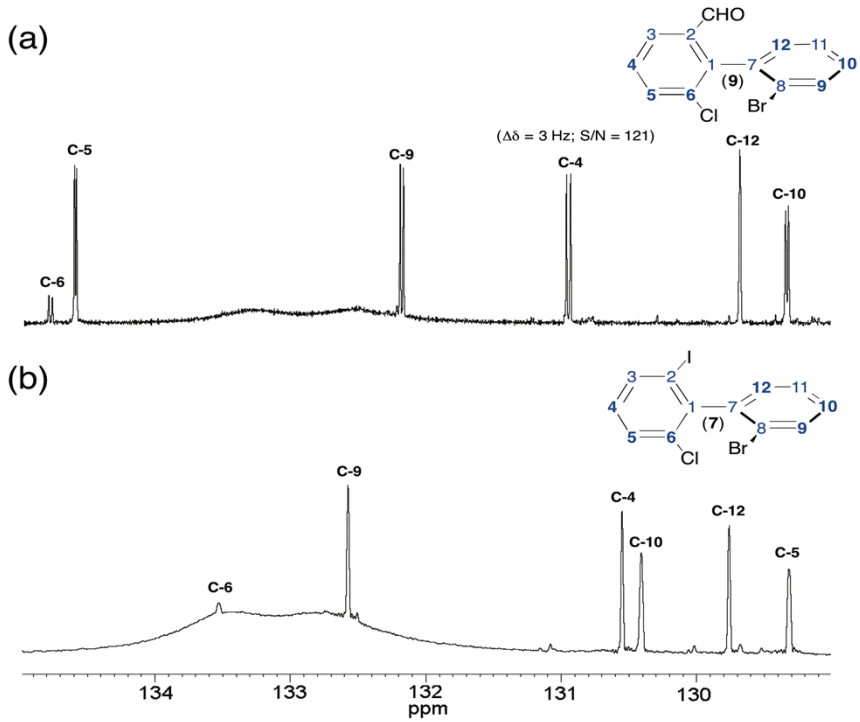

Fig. SI-7. Part of ^{13}C-{^{1}H} 1D-NMR spectrum of (*R*/*S*)**-9** and (b) (*R*/*S*)-**7** recorded in PBLG/$CHCl_3$ and entered between 129 and 135 ppm. Note the absence of enantiodiscriminations for (*R*/*S*)-**7** in the spectral range shown.

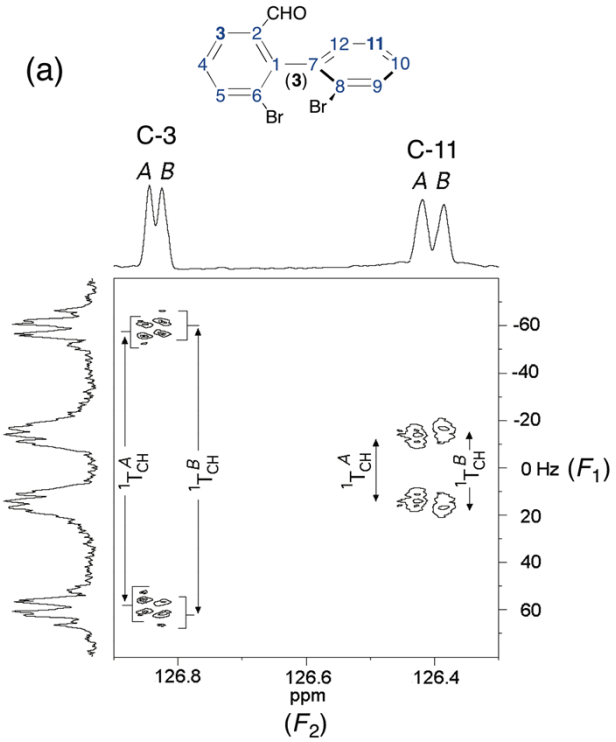

Fig. SI-8. (a) Expanded region around 126.5 ppm of the 100.6 MHz ^{13}C-^{1}H T-resolved 2D spectrum of (*R/S*)-**3** dissolved in PBLG/$CHCl_3$. The map was recorded with 2 k (t_2) × 300 (t_1) data points and 48 scans per t_1 increment. The 2D matrix was then zero-filled to 2k (t_2) × 2k(t_1) data points. Note the difference of $^{1}T_{CH}$ couplings for each enantiomer at sites C-3 and C-11. The T_{CH} values (in Hz) measured in F_1 are equal to the half of the true values. As for **6**, the spectral pattern for both sites is dominated by the direct $^{1}T_{CH}$ coupling that is different for each enantiomer ($|^{1}T_{CH}^{A/B}$(C-3)| = 234/238 Hz and $|^{1}T_{CH}^{A/B}$ (C-11)| = 66/74 Hz).

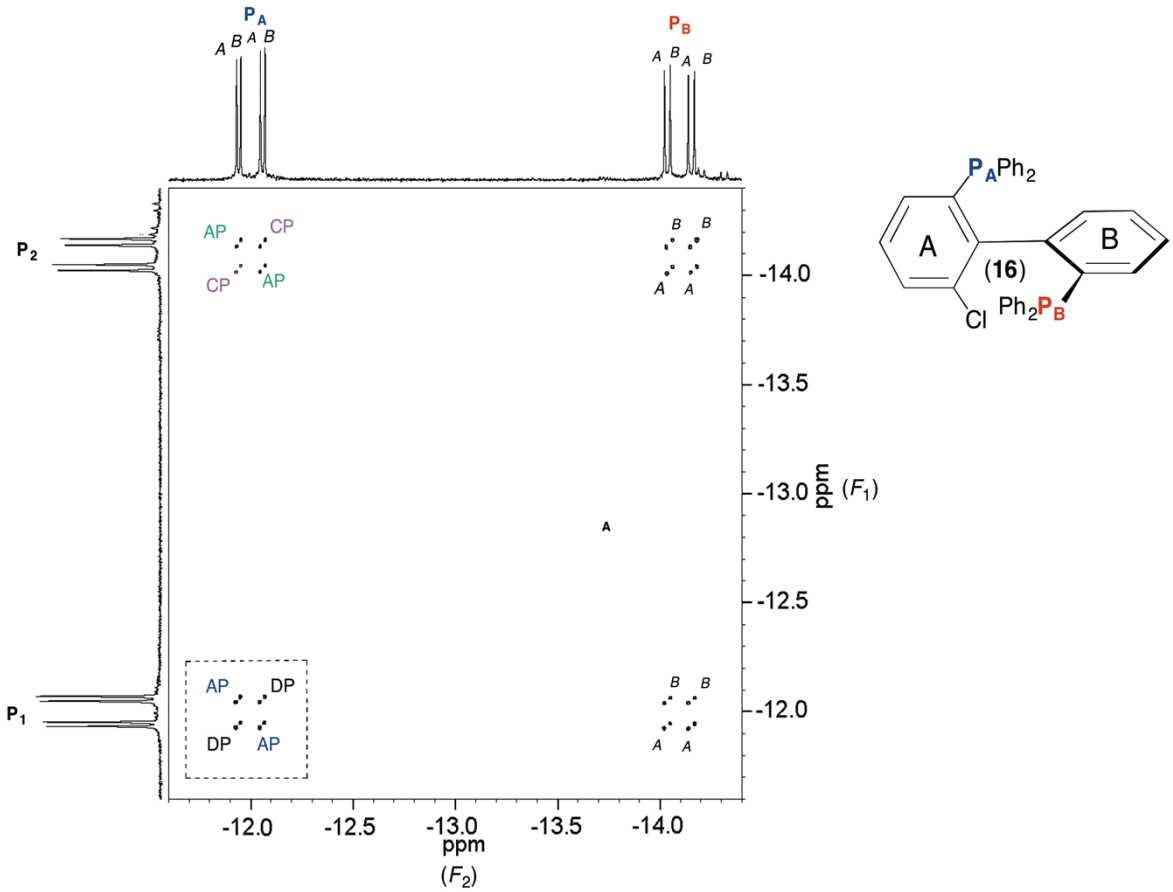

Fig. SI-9. 161.9 MHz proton-decoupled ^{31}P-^{31}P COSY 2D spectrum (phased) of (*R/S*)-**16** dissolved in PBLG/$CDCl_3$ with 1k (t_2) × 1k (t_1) data points and 2 scans per t_1 increment. The 2D matrix was then zero-filled to 2k (t_2) × 2k(t_1) data points. The map was symmetrized. As F_1 and F_2 projections, the ^{31}P-{^{1}H} 1D spectrum is displayed. The center of two pairs of doublets was calibrated at 0

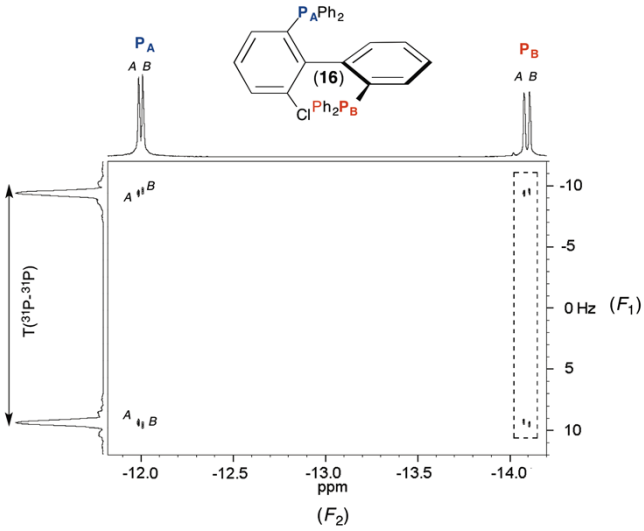

Fig. SI-10. Full 161.9 MHz proton-decoupled tilted ^{31}P T-resolved 2D spectrum (magnitude) of *(R/S)*-**16** dissolved in PBLG/$CDCl_3$ and recorded with 1800 (t_2) × 256 (t_1) data points and 8 scans per t_1 increment. The 2D matrix was then zero-filled to 2 k (t_2) × 1 k (t_1) data points. The map was symmetrized after tilting.

The true F_1 and F_2 2D projections are shown. The center of two pairs of doublets was calibrated at 0

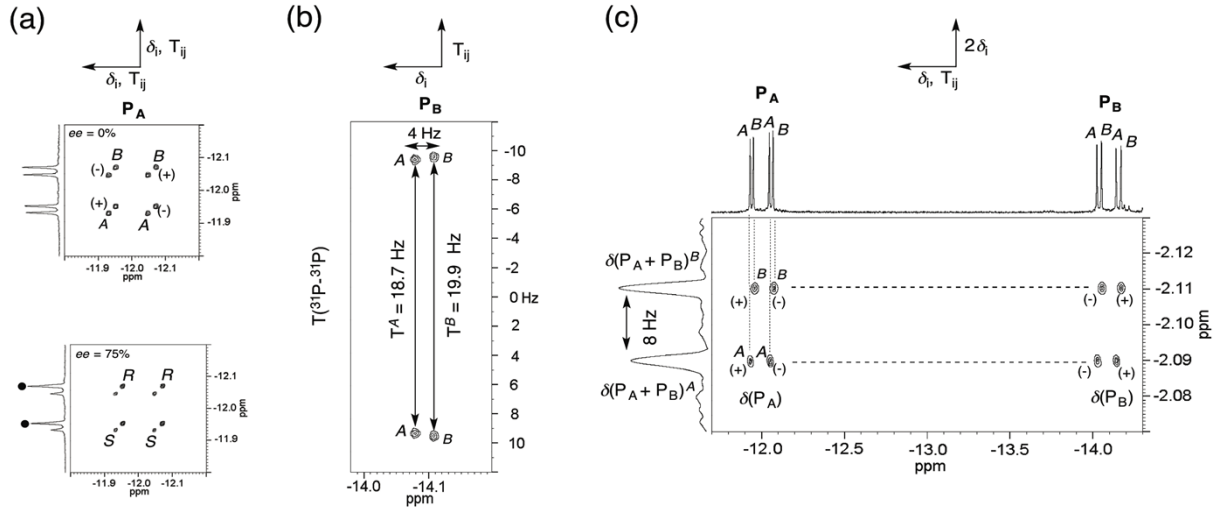

Fig. SI-11. Examples of homonuclear 2D maps of **16** dissolved in PBLG at 295 K. (a) Part of the phased ^{31}P-^{31}P COSY 2D map of (*R*/*S*)-**16** *(top) and* (*ee-R*)-**16** (bottom) at site $^{31}P_A$. (b) Part of tilted ^{31}P T-resolved 2D (magnitude) spectrum of (*R*/*S*)-**16** at site $^{31}P_B$ (see also the **Supp. Info** for details). Both maps are symmetrized (standard procedure). (c) Full phased ^{31}P-^{31}P INADEQUATE 2D spectrum of (*R*/*S*)-**16** recorded with a refocusing delay, τ□□sets at 13.2 ms. Proton decoupling is applied for each experiment. The sign of phase of peaks (+/-) is indicated.

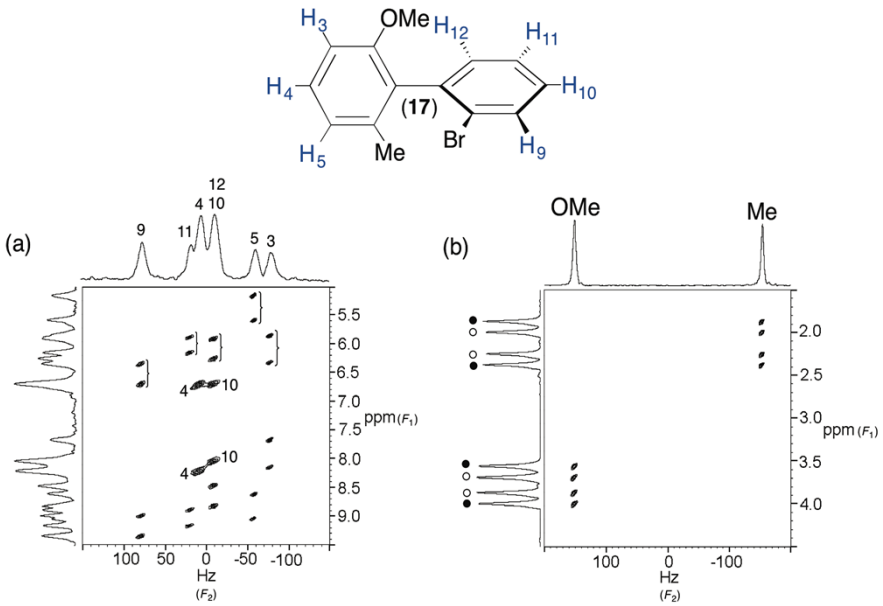

Fig. SI-12. Two expanded regions of the 92.1 MHz proton-decoupled NAD *Q*-COSY Fz 2D map centered on the (a) aromatic and (b) aliphatic regions of (*R*/*S*)-**17** dissolved in PBLG/$CHCl_3$, The spectrum has been recorded at 295 K using 1200 (t_2) × 512 (t_1) data points and 200 scans per t_1 increment (T_{exp} = 15 h). The assignment of ^{2}H DQs derives from the analysis of isotropic ^{1}H 1D/2D 1D/2D-NMR spectra in combination with assignments predicted by ACD software and increment tables. Exponential filtering (LB = 2 Hz) is applied on both dimensions.

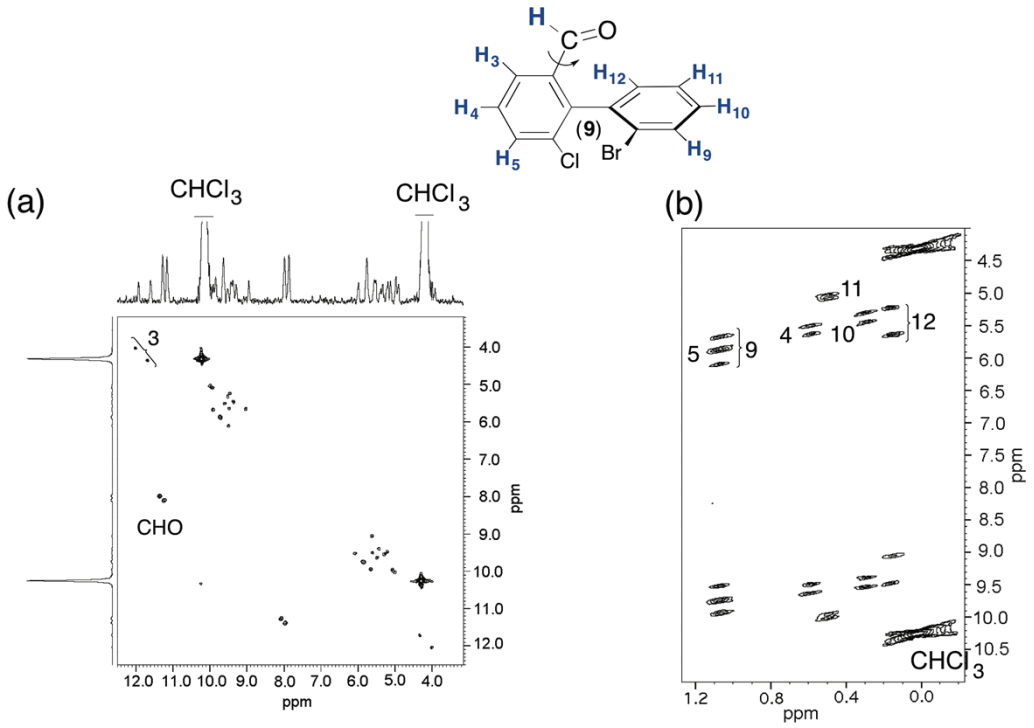

Fig. SI-13. (a) Full 92.1 MHz proton-decoupled NAD *Q*-COSY Fz 2D spectrum of (*R/S*)-**9** dissolved in PBLG/$CHCl_3$ at 295 K and recorded with 800 (t_2) × 400 (t_1) data points and 264 scans per t_1 increment. The 2D matrix was then zero-filled to 2k (t_2) × 2k (t_1) data points. The map was symmetrized. The true F_1 and F_2 projections are displayed with different vertical scale. (b) Expansion on the aromatic region of the tilted *Q*-COSY Fz map. In F_2 dimension, the signal of $CDCl_3$ was arbitrarily set to 0 ppm.

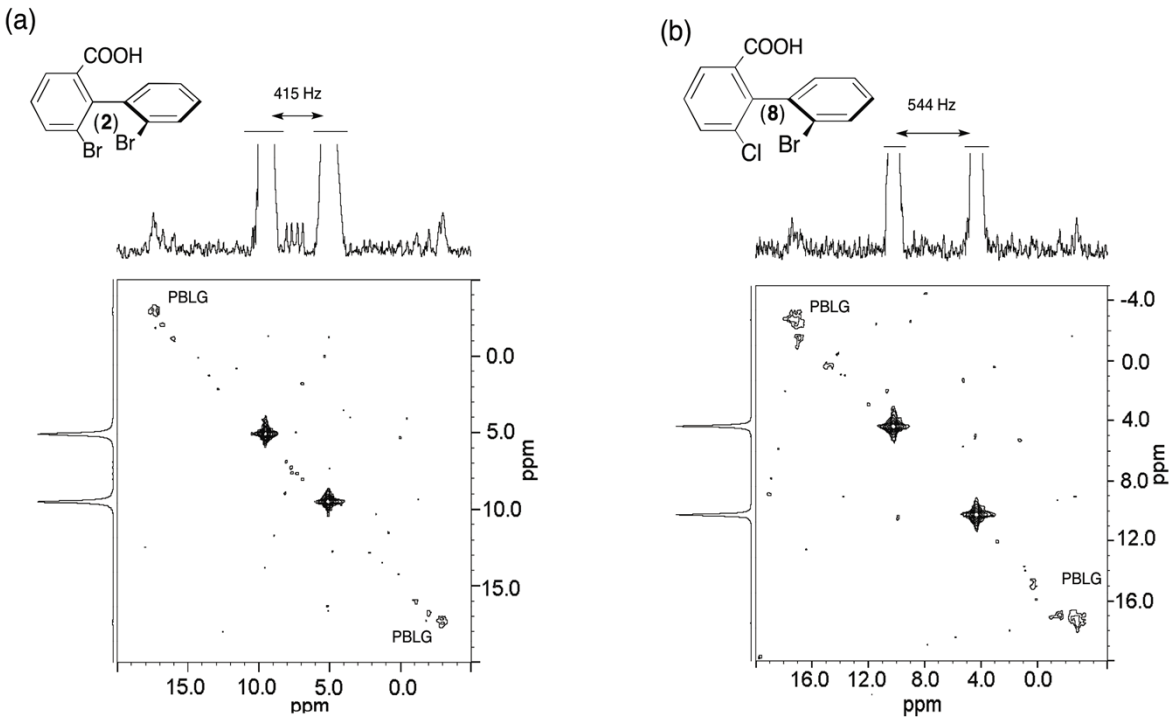

Fig. SI-14. Full 92.4 MHz proton-decoupled NAD *Q*-COSY Fz 2D spectrum of (a) (*R/S*)-**2** and (b) (*R/S*)-**8** both dissolved in PBLG/$CHCl_3$ at 295 K. Spectra were recorded with 3k (t_2) × 512 (t_1) data points and 512 scans per t_1 increment. The 2D matrix was then zerofilled to 4k (t_2) × 2k (t_1) data points. The map was symmetrized. The true F_1 and F_2 2D projections are displayed. The largest QD labelled "PBLG" arises from the aromatic NAD signals of PBLG. (b) Zoom centred on about 7.5 ppm of the tilted *Q*-COSY Fz 2D map.

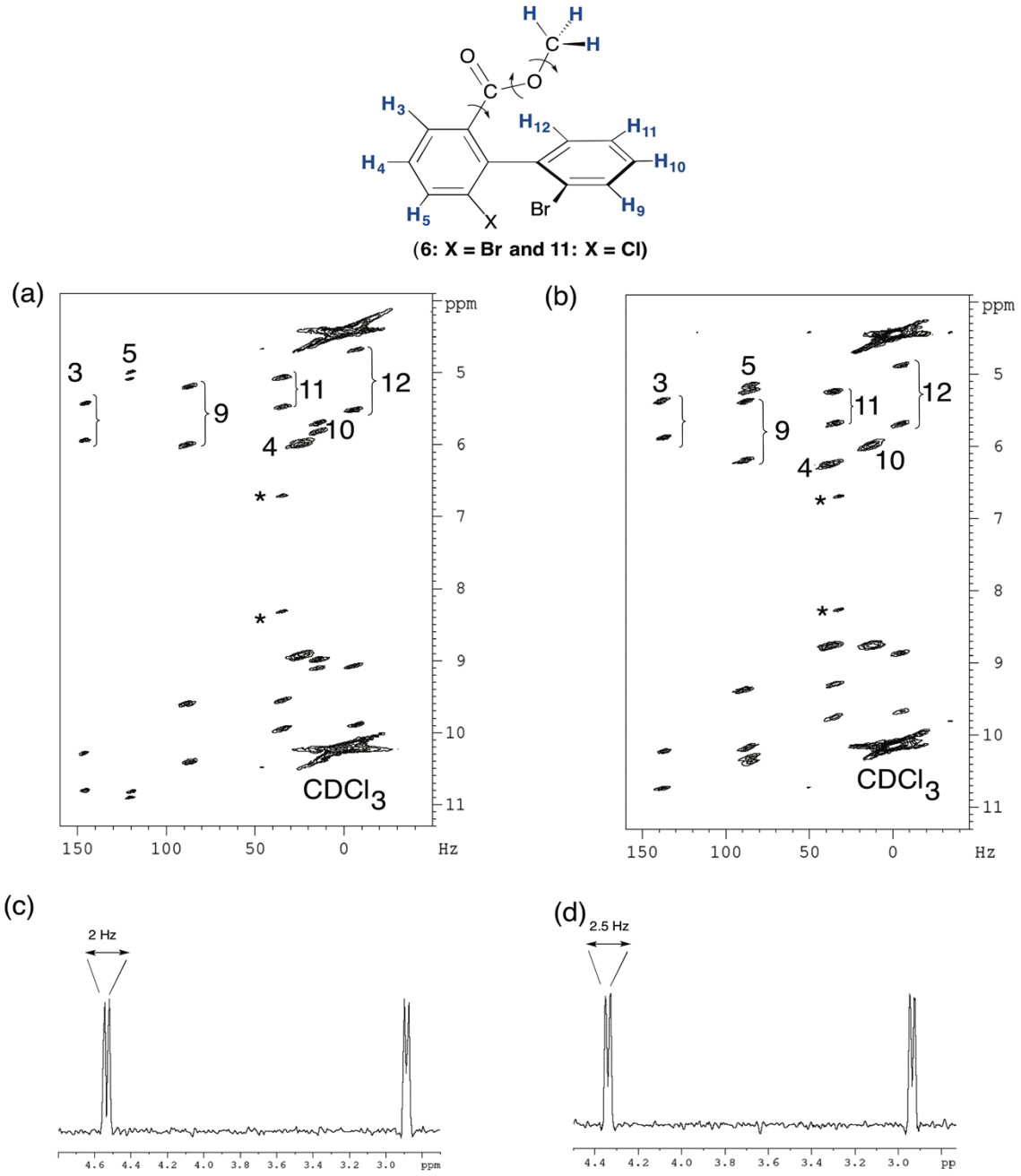

Fig. SI-15. Aromatic region of (tilted and symmetrized map) 92.4 MHz proton-decoupled NAD *Q*-COSY Fz 2D spectrum of (a) (*R/S*)-**6** and (b) (*R/S*)-**11** dissolved in PBLG/$CHCl_3$ at 295 K. NAD signals of quadrupolar doublets of the methyl group of (c) (*R/S*)-**6** and (d) (*R/S*)-**11** extracted from their associated map. Both 2D spectra were recorded with 2k (t_2) × 512 (t_1) data points and 128 scans *per* t_1 increment and then zerofilled to 4k (t_2) × 2k (t_1) data points. Exponential filtering was applied (LB = 2.5 Hz) on both dimensions. In F_2 dimension, the signal of $CDCl_3$ was arbitrarily set to 0 Hz. For (c and d), the 1D spectrum has been extracted from the tilted 2D map but here a gaussian window (GB = 0.4, LB =-3 Hz) has been applied on both dimensions prior to the double FT. NAD signals of the co-solvent impurity are marked with an asterisk.

(a)

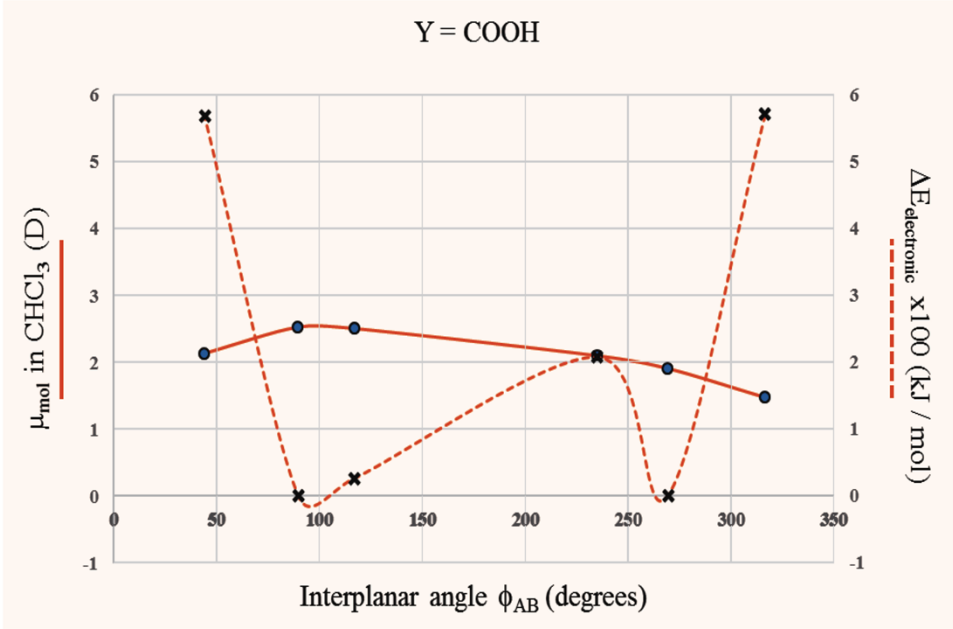

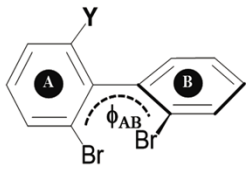

(b)

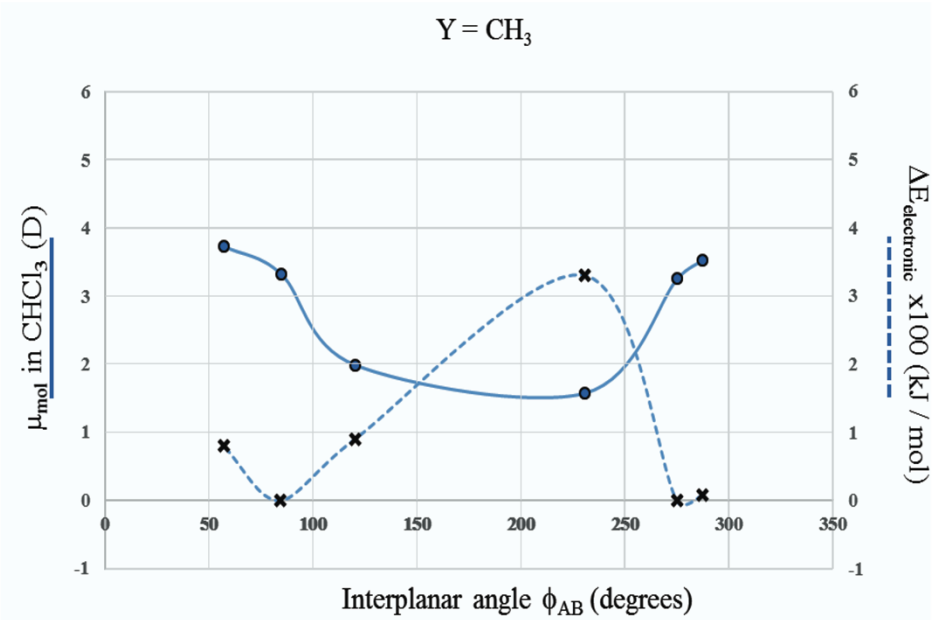

Fig. SI-16. Variation of the overall molecular dipole moment (μ_{mol}, continuous line) and the electronic energetic profile ($\Delta E_{electronic}$, dotted line) with respect to the interplanar angle redundant coordinate scanning (ϕ_{AB}) of analytes (a) **2** and (b) **5** of series **I**, considering the solvent effects ($CHCl_3$). ϕ_{AB} sign was defined as described in **Table SI-4**. Both observables were obtained by means of the redundant coordinate optimization protocol, with the same level of theory described in **Section 3.3**, main text.

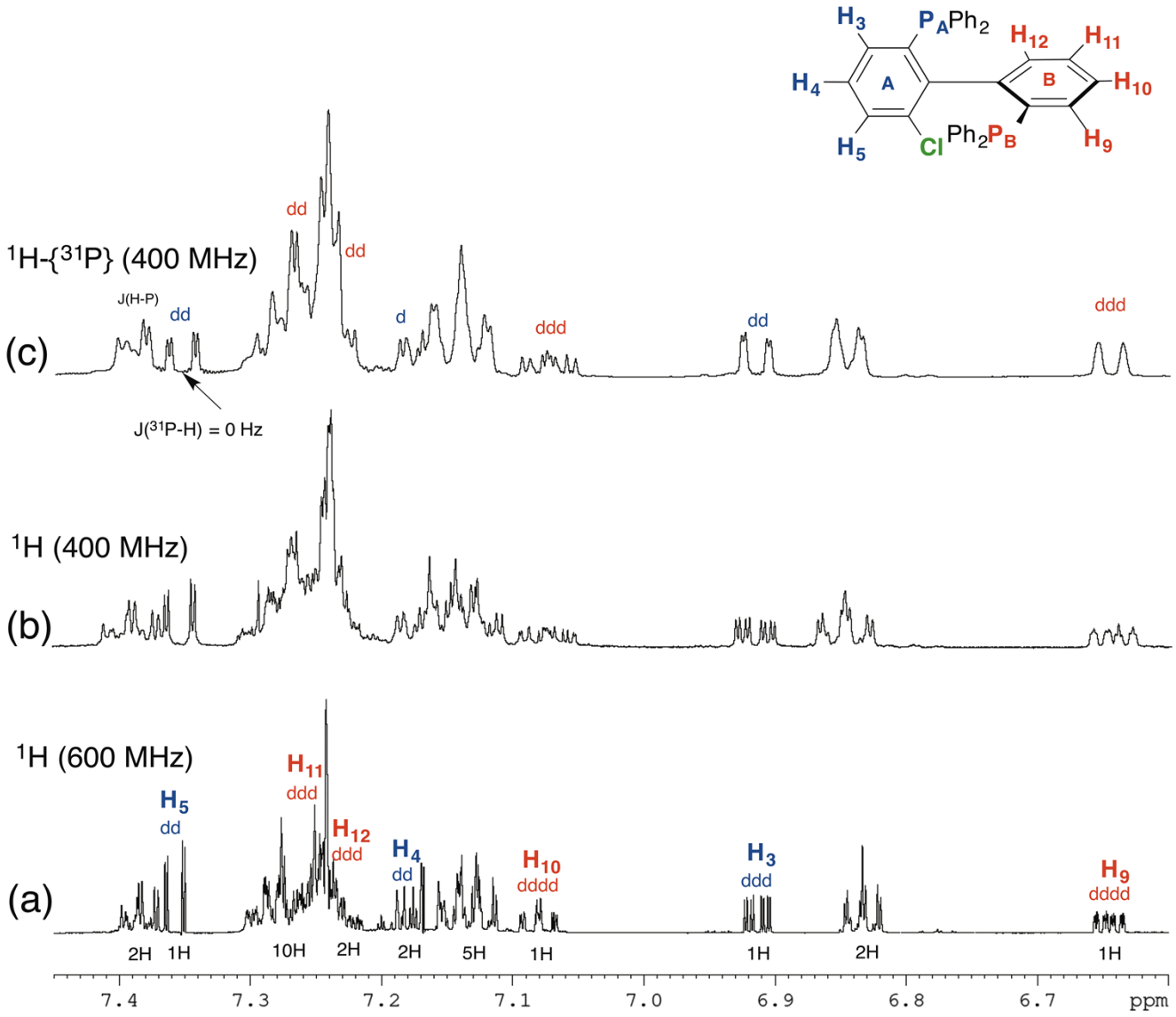

Fig. SI-17. (a and b) 400.1 and 600.1 MHz ^{1}H 1D-NMR spectra and (c) 400 MHz ^{1}H-{^{31}P} 1D-NMR spectrum of **16** recorded in $CHCl_3$ at 295 K. The number of scans added was (a) 16, (b) 16 and (c) 8. On spectrum (a), a gaussian filtering was applied to improve the spectral resolution and separate all small couplings.

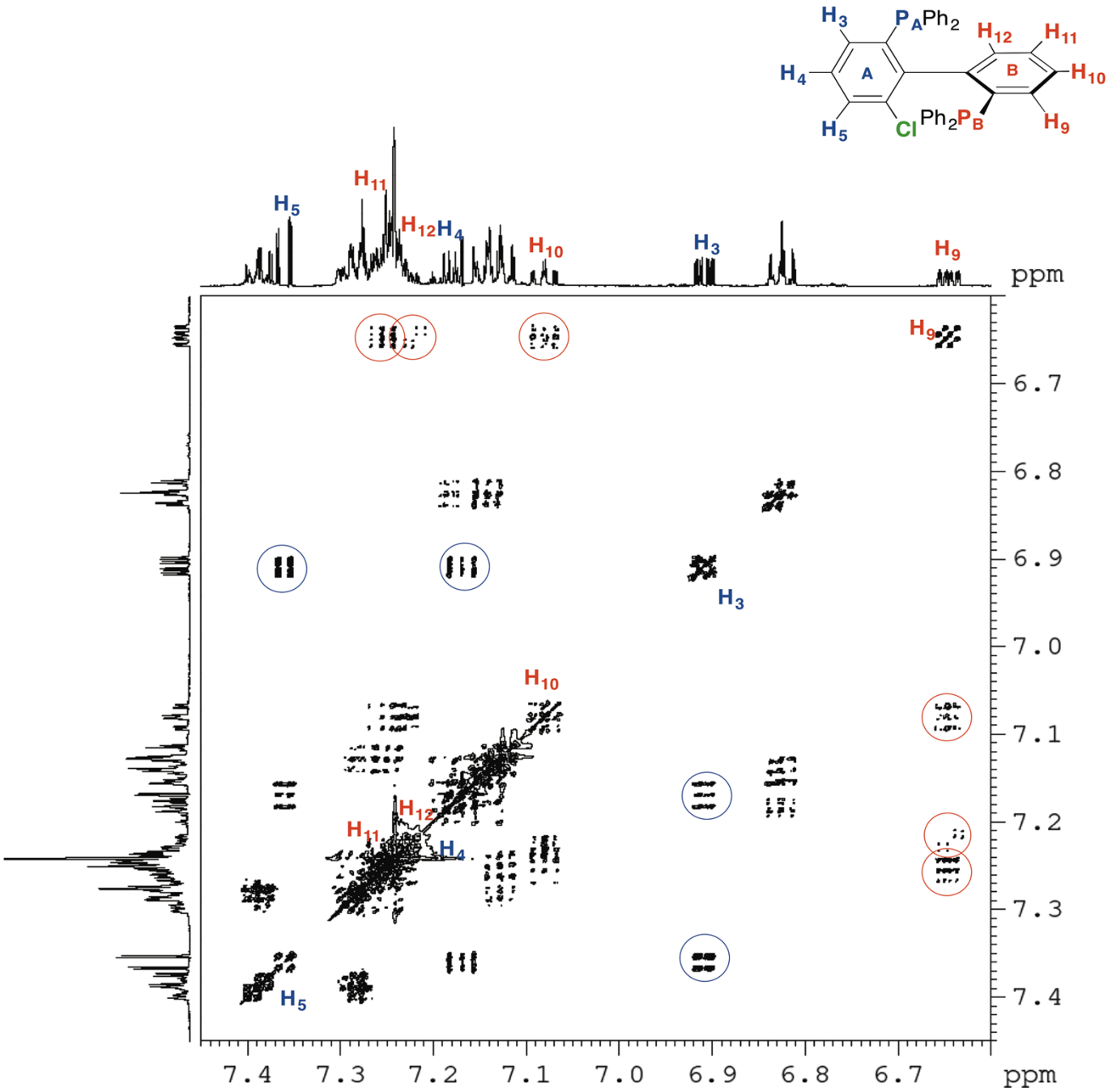

Fig. SI-18. 400.1 MHz ^{1}H-^{1}H COSY 2D spectrum of **16** recorded in $CHCl_3$ at 295 K. The 2D spectrum has been recorded with 2k (t_2) × 1k (t_1) data points and 8 scans per t_1 increment. The 2D matrix was then zero-filled to 2k (t_2) × 2k (t_1) data points and an exponential filtering is applied in both dimensions. As F_1 and F_2 projections are displayed the ^{1}H 1D-NMR spectrum (see **Figure SI-17a**).

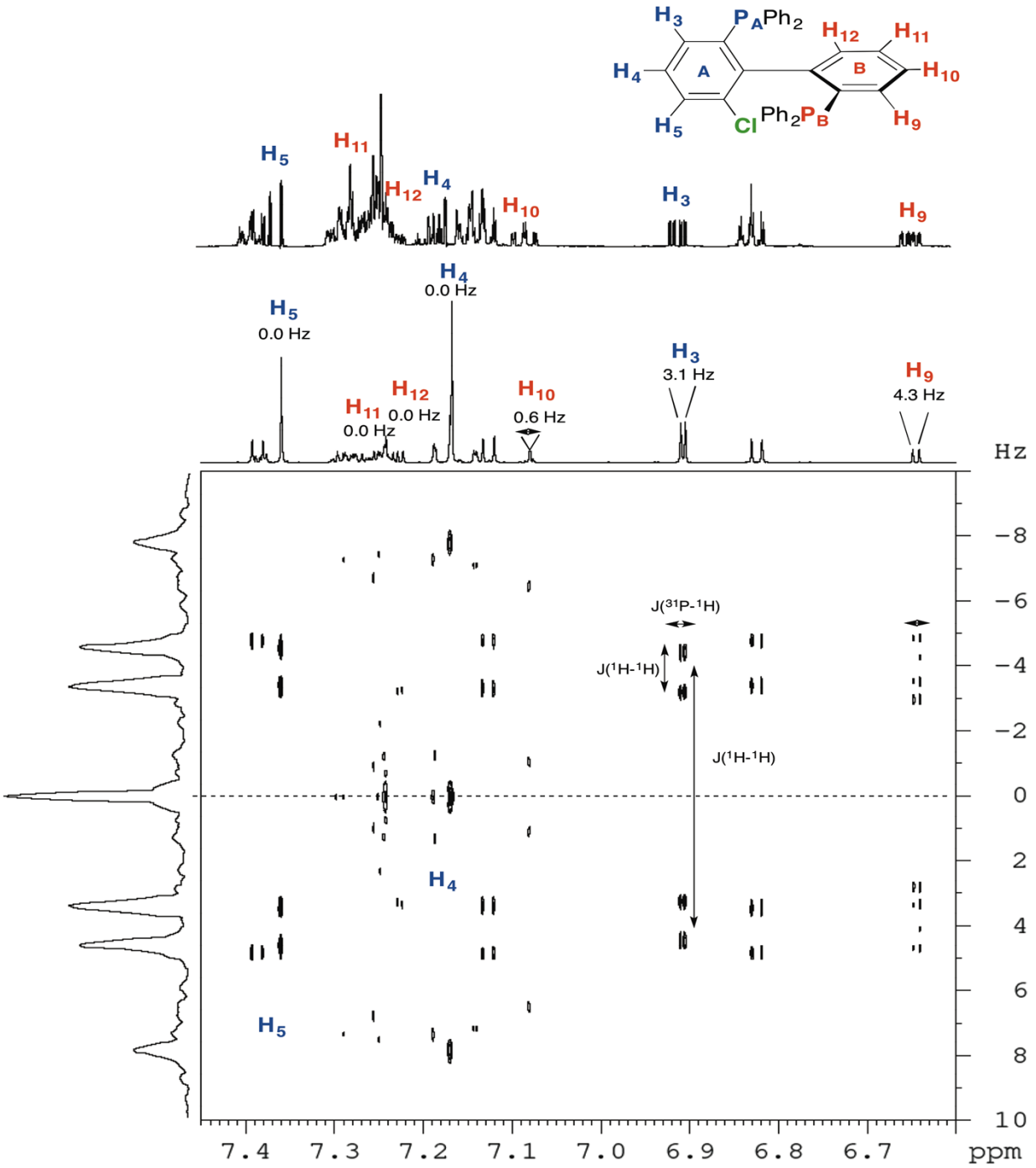

Fig. SI-19. 600.13 MHz ^{1}H-^{31}P J-resolved spectrum of **16** recorded in $CHCl_3$ at 295 K. The scalar splittings J(^{31}P-^{1}H) are observed parallel to the F_2 dimension. The 2D spectrum has been recorded with 2k (t_2) × 256 (t_1) data points and 8 scans per t_1 increment. The 2D matrix was then zero-filled to 4k (t_2) × 2k (t_1) data points and a gaussian filtering applied in both dimensions. In F_1 is displayed the true 2D projection. As F_2 projection is displayed the ^{1}H-{^{31}P} (bottom) and ^{1}H (top) 1D-NMR spectra (see **Figure SI-17**).

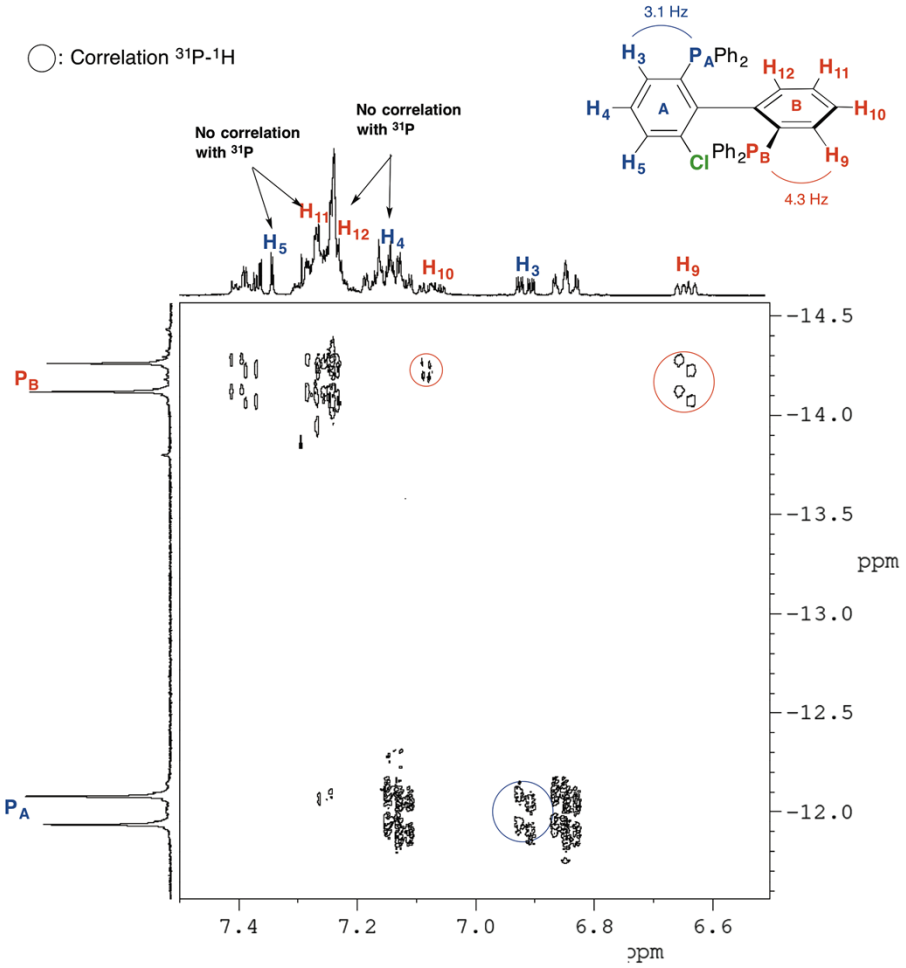

Fig. SI-20. 161.9 MHz ^{1}H-^{31}P HMBC 2D spectrum of **16** recorded in $CHCl_3$ at 295 K. Note the absence of correlation peaks for H_5 and H_{11} (*para* position relative to the ^{31}P atoms in associated rings A and B). The 2D spectrum has been recorded with 2k (t_2) × 990 (t_1) data points and 8 scans per t_1 increment. The 2D matrix was then zero-filled to 4 k (t_2) × 2 k (t_1) data points and no filtering was applied in both dimensions. As F_1 and F_2 projections are displayed the ^{31}P-{^{1}H} and ^{1}H 1D-NMR spectrum.

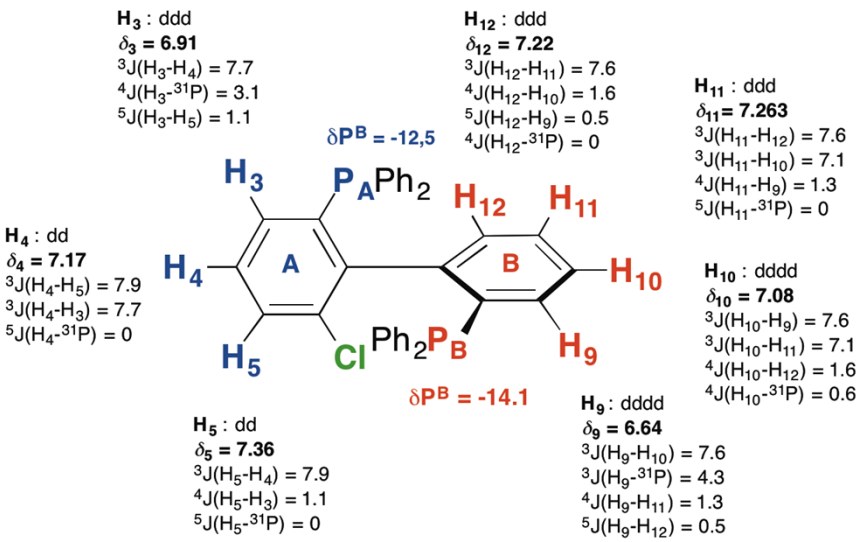

Fig. SI-21. Final spectral assignment of aromatic protons (δ_i and $^{n}J_{H-H}$ and $^{n}J_{H-P}$) in rings A and B derived from the spectral analysis of various homo- and heteronuclear 2D maps displayed from **Figures SI-17** to **SI-20**.